Powder Technology 486 (2027) 123301

Contents lists available at ScienceDirect

Powder Technology

journal homepage: www.journals.elsevier.com/powder-technology

Combined surface-based and density-based spreadability assessment of metal and polymeric powders for Powder Bed Fusion

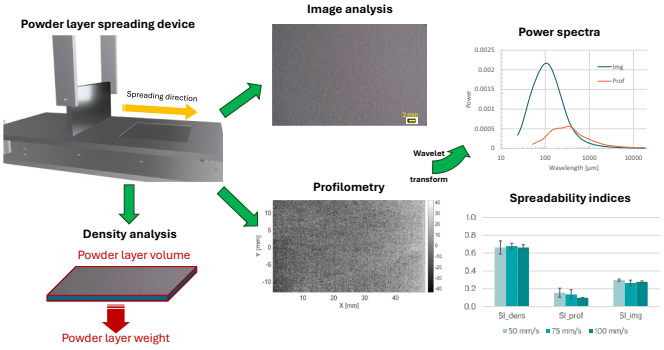
Bruno Nicola Dose [a], Sina Zinatlou Ajabshir [a], Saba Saifoori [b], Mozhdeh Mehrabi [b], Ali Hassanpour [b,*], Diego Barletta [a], Massimo Poletto [a,*]

[a] Department of Industrial Engineering, University of Salerno, Italy
[b] School of Chemical and Process Engineering, University of Leeds, UK

HIGHLIGHTS

- Spreading tests with blade tool on Ti6Al4V, AlSi10Mg, PA6 and PA6 Black.
- Internal and wall friction properties were measured and compared.
- Layer density and surface quality were assessed by three methods.
- Spreadability indices depended on material and spreading speed.
- Metals were more speed-sensitive and less variable than polymers.

GRAPHICAL ABSTRACT



ARTICLE INFO

Keywords:
Powder bed fusion
Additive manufacturing
Powder spreading
Powder layer quality
Spreadability

ABSTRACT

The quality of Powder Bed Fusion (PBF) parts relies on the quality of deposition of each powder layer. Despite powder spreadability being a key factor, no standard definition or universal Spreadability Index is currently available. Literature indices are typically based on static layer features, such as density and surface quality, or on dynamic behaviour, such as avalanche angle. Density-based indices are mainly used for metal powders, while surface-based indices are common for polymers, although they are often treated as equivalent. This study compares density- and surface-based spreadability for two metals, Ti6Al4V and AlSi10Mg, and two polymers, PA6 and PA6 Black, spread at 50, 75, and 100 mm/s. Powder layers were characterised by imaging, laser profilometry, and gravimetry. Three spreadability indices were computed, while surface parameters were obtained from profilometry maps as a reference. Images and profilometer scans were processed by wavelet transform to generate power spectra and extract a characteristic wavelength from the dominant peak. Layer density was calculated by weighing the collected powder and using the pocket area with the tool–surface gap to define the layer volume. The influence of spreading speed was strongly index- and material-dependent. For Ti6Al4V, SI_{img}, SI_{prof}, and SI_{dens} varied by 10%, 37%, and 3%, respectively; for AlSi10Mg by 20%, 0%, and 24%; for PA6 by <1%, 20%, and 14%; and for PA6 Black by 13%, 25%, and 3%. These results show that spreadability rankings depend on the selected index and, in some cases, on spreading speed.

* Corresponding authors.
E-mail addresses: A.Hassanpour@leeds.ac.uk (A. Hassanpour), mpoletto@unisa.it (M. Poletto).

https://doi.org/10.1016/j.powtec.2026.123301
Received 13 July 2026; Received in revised form 29 September 2026; Accepted 30 September 2026
Available online 3 October 2026
0032-5910/Crown Copyright © 2026 Published by Elsevier B.V. This is an open access article under the CC BY license (http://creativecommons.org/licenses/by/4.0/).

1. Introduction

Industrial applications of Additive Manufacturing (AM) are growing rapidly, driven by the environmental benefits associated with the potential reduction of material waste and lower energy demand than traditional subtractive manufacturing (SM) processes [1,2]. Among AM processes, Powder Bed Fusion (PBF) is one of the most widely studied and industrially relevant techniques. PBF is an AM technique based on powdered material. In PBF, a laser beam (PBF-LB) or electron beam (PBF-EB) is used to heat a layer of powder [3], causing the particles to partially or fully melt and bond together. Depending on the material and process conditions, building of parts may occur through sintering, typically employed for polymeric materials [4], or through complete melting, as commonly occurs for metallic alloys [5].

The PBF process is prominent due to the wide variety of materials that can be employed, including polymeric materials [6] and metal alloys [7], and the capability to produce complex geometries and intricate parts in a single process [8] at reduced design costs. Complex components can be produced directly from a digital models obtained by Computer Aided Design (CAD) [9]. AM techniques, in particular PBF, can streamline the supply chain by removing intermediate processing steps, reducing transport time, and enabling more decentralised production, thereby improving sustainability [10].

The quality of the final PBF components strongly depends on the quality of each spread powder layer [11,12]. Such dependence is mainly linked to the layer's density and surface properties, whose relative importance may vary depending on the part building mechanism. In melting-based processes, powder-bed density is frequently investigated because it influences material availability and the formation of the melt pool [13,14]. Conversely, in sintering-based processes, where the spatial arrangement of the particles is more closely retained during part building, local variations in bed height and surface irregularities may have a stronger influence on the quality and mechanical performance of the final component [15,16].

The characteristics of the produced layer and its quality, as well as the dynamic behaviour of the powder during spreading, are influenced by the material's properties [17], environmental conditions, such as temperature [18], and process parameters, such as spreading tool speed [19] and shape [20,21]. Layer quality is also strongly affected by particle morphology, since spherical particles generally provide higher packing density during spreading [22,23], whereas non-spherical particles tend to exhibit lower packing efficiency [21]. In general, spreadability refers to a powder's ability to spread into a homogeneous, uniform layer suitable for PBF processes [24]. However, spreadability is not yet standardised, and there is no universally accepted index for assessing layer quality quantitatively [25]. The literature offers several methods for evaluating spreadability, each using different measurement techniques. A first class of methods is based on powder-layer density. Layer density is generally calculated as the ratio between the mass of powder contained in the deposited layer and its geometric volume. Density-based spreadability indices commonly normalise this value with respect to a reference powder density, such as tap density (ASTM B527–24) [26]. However, the definition of the layer volume itself is not unique. When spreading is performed over a flat surface, the theoretical layer height may be related to a characteristic particle size, such as d_{90} [24]. In contrast, other approaches rely on the experimentally measured average layer height [27]. Alternatively, a pocket of uniform depth carved on a flat surface is employed to simulate the spacing generated by the tray's movement in an actual commercial machine. In this case, the height is determined by the pocket depth and the gap between the spreading tool and the underlying surface [13].

Since in situ measurement of layer density can be challenging, surface-based spreadability metrics have also been extensively investigated. These methods generally quantify surface irregularities using parameters directly or indirectly related to roughness and make use of non-intrusive acquisition of information on the powder-bed surface. Image-analysis methods, for example, can identify macroscopic defects and quantify their severity according to their size and position within the layer [28]. Optical profilometry can also be employed to characterise surface topography. Yim et al. [29] used 3D optical measurements to acquire height data of the entire surface and calculate surface roughness (S_a). Other approaches include electron-optical imaging in PBF-EB systems, where backscattered-electron signals can be used to reconstruct layer topology [30], and X-ray transmission imaging, which has been employed to estimate local effective powder depth and evaluate surface uniformity [31]. Sehhat et al. [32] used a laser profilometer to measure line roughness, R_a, at the centre of a spread powder, which was related to the surface quality [32]. In other studies, shadows were generated by applying grazing light to the layer surface, and the layer image was analysed to obtain information on surface quality related to the shadow length [33]. Zinatlou et al. [18,34] assessed layer quality using grazing-light images (converted to grayscale) and wavelet analysis of line profiles to obtain power spectra; the dominant peak defined the characteristic wavelength pl. Spreadability was quantified as $SI = d_{50}/pl$, where a higher SI indicates better surface quality. It was also found that spreadability can be associated with the powder particle Bond number [29,30], which accounts for the relevance of interparticle forces at the particle level. It is defined as

$$Bo = F_{IP}/W \tag{1}$$

where F_{IP} is the interparticle force, and W is the particle weight. A system with $Bo > 1$ is dominated by interparticle forces; the opposite is true for $Bo < 1$. Shear testing was used to estimate the Bond number for polymeric powders quantitatively.

Despite extensive efforts reported in the literature to quantify powder spreadability using different indices, the coherence of the various approaches has not been systematically studied. Density- and surface-based parameters are often considered equivalent spreadability indicators [35], although they may describe different aspects of the powder layer. Powder layer density is commonly correlated with the final part density in PBF, particularly in sintering-based techniques [22]. However, product quality also depends on buildability and geometrical consistency, which may be affected by the continuity between consecutive layers and, therefore, by layers' surface characteristics [36]. Additionally, the powder layer's density is not able to return local characteristics of the layer crucial for the correct assessment of the spreadability. For example, small but deep flaws, or long but shallow flaws, may result in negligible changes in the powder layer's density but cause substantial defects on the final item, especially if the flaws are positioned in areas where the laser will interact with the powder. These apparently small defects may cause brittleness of the item, or they may accumulate in the subsequent layers, increasing the severity of the defect [37]. On the other hand, the surface analysis is useful to identify the characteristics of the interface between two consecutive layers and has the advantage of being potentially used as a monitoring tool of the process. However, the surface analysis is not sufficient to determine the internal characteristics of each layer. In fact, it is challenging to derive from surface characterisation only information such as the layer void fraction or the particle arrangement. The risk is to obtain layers with an assumed satisfactory interface corresponding, however, to a poor bulk density, which may result in poor mechanical properties in the final item. Moreover, comparisons among different spreadability metrics are commonly performed across separate experiments, materials, or spreading conditions, making it difficult to determine whether discrepancies among indices arise from the measurement principle itself or from differences in the investigated powder bed.

This work investigates the differences between density- and surface-

based spreadability indices for polymeric and metallic powders and assesses whether direct mathematical or statistical correlations exist among them. Powder layers of two metallic materials, Ti6Al4V and AlSi10Mg, and two polymeric materials, PA6 and PA6 Black, were spread at 50, 75, and 100 mm/s and characterised through density measurements, grazing-light shadow imaging, and laser profilometry. Unlike similar research in the literature, the simultaneous application of these complementary techniques enables a direct comparison of their ability to discriminate between materials and spreading conditions. In particular, density-based and surface-based descriptors are evaluated concurrently, allowing their mutual consistency and sensitivity to material and process conditions to be assessed without the confounding effect of independently produced powder beds. In addition, the new modified grazing-light image-analysis approach is applied together with density measurements and laser profilometry to extract quantitative information from the same powder bed. This combined application enables a direct comparison of surface heterogeneity and layer filling under identical spreading conditions, while retaining the potential for rapid and non-intrusive process monitoring.

2. Materials and methods

2.1. Powders and properties

In this work, four powders specifically produced for PBF-LB processes were tested. Materials consist of two metal powders and two polymeric powders. The metal powders are Ti6Al4V and AlSi10Mg fine powders, both produced by *Renishaw plc*. Polymeric powders are two polyamides: PA6 (*Sinterline®* by *DOMO Chemicals GmbH, Germany)* and PA6 Black powder (*BASF 3D Printing Solutions GmbH, Germany)*. The latter is made of polyamide particles coated with carbon black fines. The main physical properties of the four powders are reported in Table 1. The bulk density of the metal powders was measured using an FT4 Powder Rheometer (*Freeman Technology, Tewkesbury, UK*) at the University of Leeds. For the polymer powders, bulk density was measured using an envelope and density analyser (*GeoPyc 1365, Micromeritics, Norcross, Georgia, USA*) at the University of Salerno. Table 1 shows that metal powders have particle densities roughly 2–4 times higher than polymer powders. Particle densities were reported by manufacturers. Diameter percentiles in Table 1 were extracted directly from the powders' Particle Size Distributions. In the case of polymeric powders, PSDs were obtained through a Malvern Instruments-Laser diffraction method in a wet environment following Mie theory (*Mastersizer Hydro 2000S, Malvern, UK*) at the University of Salerno; metal powders' PSDs were measured through an Anton Paar-Laser diffraction method in a dry environment following Mie theory (*QICPIC/L-RODOS/L, M5, Anton Paar GmbH, Austria*) at the University of Leeds.

The shape and geometry of the powders were examined using SEM analysis. Hitachi TM3030Plus (*Hitachi, Tokyo, Japan*) was used for the metal powders at the University of Leeds, and FESEM LEO 1525 (*Carl Zeiss SMT AG, Germany*) was used for the polymer powders at the University of Salerno [34]. Ti6Al4V powder particles appear as highly spherical with sporadic satellites on the surface, as shown in Fig. 1a. AlSi10Mg powder particles are mainly spherical and elongated, with some fines often appearing as satellite particles adhering to the surface of the coarser ones (Fig. 1b). Among the polymer powders, PA6 particles are very irregularly shaped and range widely in size. Many of them are elongated and have sharp, angular shapes (Fig. 1c). PA6 Black particles have smoother oval shapes, without many fines (Fig. 1d).

Table 1
Physical properties of powder used as experimental materials.

Materials	ρ_p $[kg/m^3]$	ρ_b $[kg/m^3]$	d_{10} $[\mu m]$	d_{50} $[\mu m]$	d_{90} $[\mu m]$
Ti6Al4V	4510	2430	16	33	52
AlSi10Mg	2660	1389	27	40	59
PA6	1130	525	15	46	91
PA6 Black	1370	690	40	74	129

2.2. Methodology and analysis

2.2.1. Flow properties

Internal shear tests and wall shear tests were conducted for each powder to evaluate its internal cohesion and adhesion to the contact wall, corresponding to two system properties involved in the powder spreading process.

2.2.1.1. Internal yield loci and flow function. An Anton Paar MCR 302 WESP (Anton Paar GmbH, Graz, Austria) was used to perform shear tests at different consolidation conditions and at room temperature. The annular trough of the shear tester, with an internal volume of approximately 19 cm^3, was filled with the powder and then levelled. The filled trough was placed in the shear tester holder, and the test was then started. A vaned lid was lowered onto the powder surface in the trough to begin the measurement. Alternated pre-shear and shear steps were performed to measure static yield loci and derive the flow function of the powders, as the unconfined yield strength, f_c, versus the major principal stress, σ_1, and the corresponding cohesion at different consolidation stresses. The normal stresses during the pre-shear steps were set at 1, 2, 4, and 8 kPa. Cohesion, C, angle of internal friction, Φ_i, dynamic angle of internal friction, Φ_e, and unconfined yield strength, f_c, were derived as a function of major principal stress, σ_1, under different consolidation conditions and used to extrapolate cohesion at major principal stress similar to spreading conditions, with low normal loads. Shear tests were conducted on every powder, performing three repetitions for each condition.

2.2.1.2. Wall friction. The Anton Paar MCR 302 WESP was also used to perform wall shear testing on each powder. For the wall friction test, the procedures for filling, levelling, and placing the filled trough in the shear tester were the same as those described for the internal shear test in Section 2.2.1.1. However, instead of using a vaned lid, an annular aluminium coupon attached to the lid was used to measure wall friction. An aluminium coupon was chosen as representative of the wall of the pocket bed employed during the spreading tests. Tangential stresses at steady state were measured at specified increasing normal stresses specified as 0.4, 0.8, 1.2, 1.6, and 2 kPa, to calculate the wall yield locus of each powder and their respective adhesion, τ_{ad}. Three repetitions were performed for each powder.

2.2.2. Spreading testing

The experiments were carried out using the spreading device developed at the University of Leeds [13], with the pocket-bed surface setup. This device includes a rack that holds the spreading tool fixed in place, and a moving platform controlled by a step motor and a screw for one-directional movement. It can be used with both flat and pocket bed surfaces by attaching a specially shaped plate to the moving platform [13]. The pocket bed is an aluminium plate with a carved rectangular area, rounded at the corners. The rectangle measures 35 mm by 50 mm and has a depth of 100 μm (Fig. 2b). While the camera acquisition allowed the acquisition of the entire pocket bed surface, the laser only allowed the acquisition of the surface properties in a rectangular area of about 50 × 20.25 mm, as shown in Fig. 2c.

In the experiments, a 60° steel blade (Fig. 2d) was chosen as the spreading tool, a V-shaped knife with an angle of 60° between the two blades' sides and the horizontal plane. Tests were performed at 21–23 °C and 28–45% relative humidity, using spreading speeds of 50, 75, and 100 mm/s. These speeds were chosen to match the order of magnitude of spreading speeds used in commercial PBF machines. Each speed–material combination was repeated three times. To ensure consistent measurements and avoid jamming [38], the blade to bed gap was selected

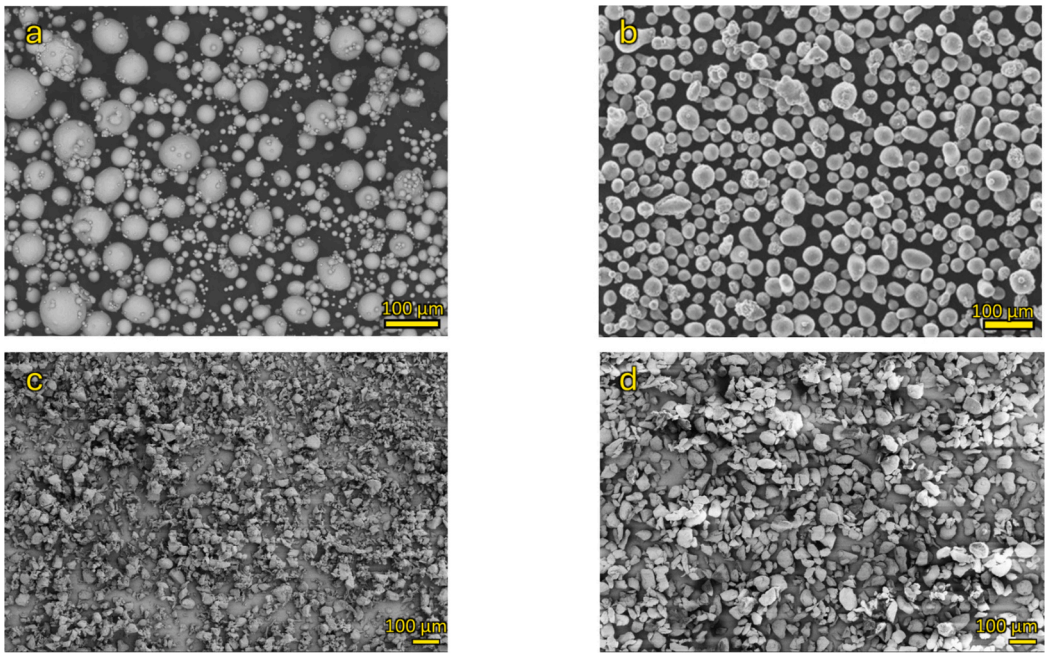


Fig. 1. SEM images of testing materials: a) Ti6Al4V metallic powder; b) AlSi10Mg metallic powder; c) PA6 polymeric powder; d) PA6 Black polymeric powder.

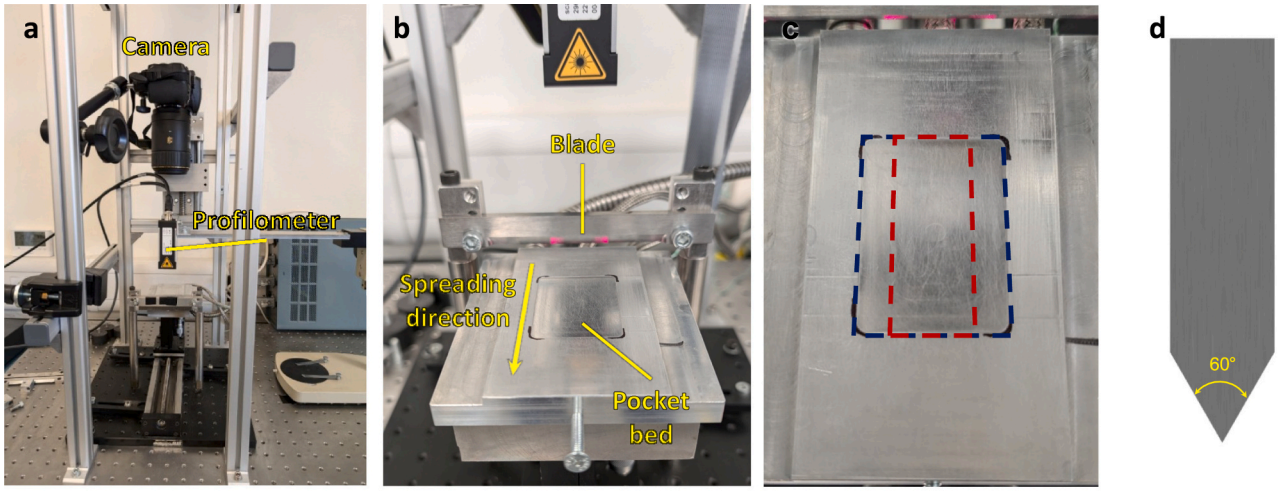


Fig. 2. Experimental setup: a) spreading table with acquisition devices; b) detail of the pocket bed in the spreading table; c) pocket bed's area acquired by photography in blue and profilometry in red; d) cross-sectional profile of the blade spreading tool. (For interpretation of the references to colour in this figure legend, the reader is referred to the web version of this article.)

during preliminary set-up calibration and was maintained at a value greater than or equal to $3d_{50}$ for Ti6Al4V, AlSi10Mg, and PA6. Accordingly, a gap of 151 µm was used for these powders. For PA6 Black, a smaller relative gap of 176 µm, corresponding to approximately $2.4d_{50}$, was found during the set-up calibration to be sufficient to obtain a consistent and complete layer.

2.2.3. Acquisition methodologies

The spread layer was characterised using various methods, each requiring a different acquisition technique.

The first set of data was collected using a 24 MP camera, the D3300 *(Nikon, Japan)*, with a 105 mm macro lens, the f/2.8 DG MACRO HSM (*Sigma, Japan*). This setup captured high-resolution images of the spread powder layer for image analysis. In this step, an LED beam projector was placed at a 45° angle to shine across the surface of the spread layer. Surface roughness, hit by grazing light, created shadows, whose length depends on the height and width of peaks and on the size of the associated particle clusters, helping to assess surface quality. The captured image was then converted to grayscale so that pixel intensity could be used for image analysis. The image pixel covered an area of about 9 µm size and was therefore smaller than the average particle size.

The second acquisition procedure used a laser profilometer to scan the spread powder layer (Scancontrol 2960–25 v48–15, Micro-Epsilon-Messtechnik GMBH & CO. KG, Germany). The laser is positioned vertically above the setup and is oriented perpendicular to the spreading direction. So, defining as x the horizontal spreading direction, y the horizontal direction orthogonal to it and parallel to the blade and z the vertical direction to the blade, the profilometer allows the acquisition of a line composed of 1280 points of z values over 20.25 mm in the y direction. This vertical dimension is obtained from the 2D rendering internally made by the profilometer's acquisition software, hence is affected by the transformation of the bins into pixels, resulting in a

stretched *y* dimension. For this reason, the vertical dimension of the bins shouldn't be calculated by the rendered image without knowing the stretching factor. The stretching factor was calculated comparing the scanning map with the actual layer image, and it was found to be equal to 1.12. These profiles were collected while moving the spreading device at approximately 2.7 mm/s in the *x* direction, covering the whole 50 mm length of the spread layer. The spread powder layer was scanned starting from the edge of the pocket at the aforementioned speed. Each scan recorded 2630 profiles, with 1280 points per profile, producing bins of 19.0 μm × 14.1 μm ($x \times y$) and therefore approximately three times larger than the images' pixel size, with an expected loss in resolution of the layer profile from the profilometer. Profiles were normalised over a reference surface. The reference surface was obtained in each test by calculating the moving average along each row of the profile (in the spreading direction). This process allowed the removal of any potential interference from the pocket bed tilting in a direction orthogonal to the spreading, without altering the reciprocal positions of peaks and valleys in the spreading direction.

The final step was to weigh the powder layer to calculate bed density. Excess powder was first removed, leaving only the material inside the pocket. This powder was carefully collected in a tray and weighed on an analytical scale. The layer volume was taken as the pocket area multiplied by the sum of the pocket depth and the blade–surface gap set for the test.

2.2.4. Data processing

2.2.4.1. Image analysis. Images acquired by the camera were processed to obtain a power spectrum referred to the characteristic wavelengths appearing in the distribution of shadows in the image of the spread layer. The image is cropped to remove any portion outside the pocket. Subsequently, the image was converted from RGB to grayscale. The derived pixel intensities were taken as the parameter to be analysed [39]. From the two-dimensional matrix reporting the grey level of each pixel, vectors corresponding to the grey levels in pixel rows were extracted. For this analysis, the rectangular image was divided into 4000 horizontal rows, each spanning the full length in the spreading direction. Each row was processed with a wavelet transform (Wavelet Toolbox, MATLAB®) to generate a power spectrum, using the Morlet mother wavelet. The scale and shift factors of the wavelet transform were automatically determined by the Wavelet Toolbox in the function's routine, achieving the most suitable overlapping between the original and the processed signals [15,34]. The Morlet mother wavelet was selected after a calibration step, resulting in the most reliable mother wavelet to faithfully represent the original signals. An overall power spectrum was then obtained by cumulating the single spectra from each stripe, representing the overall characteristics of the entire image. The resulting spectrum was analysed by extrapolating its main peak and width. Distances between points in the spreading direction were used to calculate relevant wavelengths starting from spatial frequencies provided by the procedure.

2.2.4.2. Profile analysis. Profiles acquired by the profilometer were analysed using a two-dimensional matrix of surface heights over the bed surface. Vectors representing these heights along stripes in the spreading direction were extracted from the 2D matrix using an approach similar to that adopted for image analysis. An interquartile range (IQR) filter was applied to remove outliers caused by random reflections from the laser interacting with the metal plate and blade. The scan was segmented into 1280 vertical stripes aligned with the spreading direction. The height values in each stripe were processed, as in the image analysis, to compute a power spectrum per stripe. An overall spectrum was then obtained by cumulatively combining the stripe spectra and analysed using the same procedure.

2.2.4.3. Surface roughness. The standard surface roughness, S_a, was used as a reference for surface quality. The standard definition assumes that the zero plane coincides with the mean plane of the surface. In this study, profilometer heights were referenced to a zero plane at the pocket bottom; therefore, a shift was required [40]. The data were re-referenced to the mean surface plane $\bar{z}$, computed as the outlier-free average of all height samples in the scan matrix shown as follows:

$$S_a = \frac{1}{M \cdot N} \sum_{i=1}^{M} \sum_{j=1}^{N} |z_{i,j} - \bar{z}| \tag{2}$$

Where *M* and *N* are respectively the number of columns and rows of the height matrix, $\bar{z}$ is the mean plane of the surface, and $z_{i,j}$ are the height points of the matrix.

2.2.4.4. Root mean square height. Root mean square height is a surface parameter employed in the calculation of superficial Skewness and Kurtosis [40]. In analogy to Eq. (2), this parameter needs to be shifted according to the average plane and discretised on the points of the scan matrix:

$$S_q = \sqrt{\frac{1}{M\,N} \sum_{i=1}^{M} \sum_{j=1}^{N} \left(z_{i,j} - \bar{z}\right)^2} \tag{3}$$

2.2.4.5. Skewness. The skewness parameter measures the symmetry of the profile. A S_{sk} index equal to 0 indicates a symmetric distribution of height in the profile and an even number and similar amplitude of peaks and valleys, whilst a positive skewness refers to profiles with high peaks and shallow or few valleys, and a negative skewness refers to profiles presenting deep valleys or scratches and removed or low peaks [40]. Shifting and discretising, the equation can be rearranged as:

$$S_{sk} = \frac{1}{M\,N\,S_q^3} \sum_{i=1}^{M} \sum_{j=1}^{N} \left(z_{i,j} - \bar{z}\right)^3 \tag{4}$$

2.2.4.6. Kurtosis. The kurtosis parameter describes the sharpness of the probability density of the profile. A S_{ku} index larger than 3 indicates a leptokurtic distribution, characterised by many high peaks and deep valleys, while an index smaller than 3 indicates a platykurtic distribution, characterised by smoothed peaks and valleys [40]. The equation, shifted and discretised, is expressed as:

$$S_{ku} = \frac{1}{M\,N\,S_q^4} \sum_{i=1}^{M} \sum_{j=1}^{N} \left(z_{i,j} - \bar{z}\right)^4 \tag{5}$$

2.2.4.7. Amplitude density distribution. The amplitude density distribution estimates the probability density function of the ordinate $z(x,y)$ within the surface where the profile is defined [41].

The amplitude density distribution was combined with kurtosis, skewness, and S_a parameters to provide a reference in surface quality, following a standard approach usually employed in tribology.

2.2.5. Indices

2.2.5.1. Image analysis spreadability index. An image analysis spreadability index, SI_{img}, was used, similar to the one suggested by Zinatlou et al. [18]. It is defined as

$$SI_{img} = \frac{d_{50}}{pl_{img}} \tag{6}$$

Where d_{50} is the 50th percentile of the tested powder Particle Size Distribution (PSD), and *pl* is the characteristic wavelength extracted as the peak wavelength of the power spectrum produced after the wavelet transform processing. In this work, the characteristic wavelength was

extracted from the overall wavelet, as described in Section 2.2.4.1. It is hypothesised that in the layer image, the variations in grey levels are related to the shadows of surface undulations. Therefore, the characteristic wavelength identified by the wavelet transform should be larger than or equal to the particle size. Therefore, it is expected that SI_{img} mostly ranges between 0 and 1 and cannot be larger than 1. Smoother layers produce smaller shadows, resulting in a lower *pl* and higher index. Consistently an increase in this index is associated with increasing surface quality.

2.2.5.2. Profile spreadability index. In analogy to SI_{img}, in this work, a similar index was calculated from the surface profile map. This profilometry-derived index, SI_{prof}, is defined, by analogy with Eq. (6), as follows:

$$SI_{prof} = \frac{d_{50}}{pl_{prof}} \tag{7}$$

In this case, a value of pl_{prof} was extracted from the profile power spectrum. The characteristic wavelength represents the spacing between surface peaks. Owing to discretisation, the wavelet analysis is limited by the profile bin size, which lies between d_{10} and d_{50} for all materials except PA6 Black. Consequently, similarly to what happens for SI_{img}, $SI_{prof} > 1$ ($pl_{prof} < d_{50}$) would occur only if the layer surface was mostly composed of sub-d_{50} particles aligned at the same height. Under these constraints, the profilometry-based spreadability index, SI_{prof}, is expected to range from 0 to 1.

2.2.5.3. Density-based spreadability index. Also, a density-based spreadability index, SI_{dens}, was adopted. As suggested by Mehrabi et al. [13], it is defined as:

$$SI_{dens} = \frac{Spread\ layer\ density}{Reference\ bulk\ density} \tag{8}$$

The spread layer density is defined as the mass of the spread layer divided by its volume. While the mass was unambiguously measured by weighing the powder deposited to form the layer, the layer volume may be defined differently. In this work, the volume of the powder layer was defined as

$$V = S_{pocket} \cdot (w + \delta) \tag{9}$$

where S_{pocket} is the surface area of the carved pocket, equal to 1736 mm^2 in the device employed for the experiments, w is the carved pocket depth, and δ is the gap between the working plate and the blade rim. The total distance ($w + \delta$) was 151 μm for Ti6Al4V, AlSi10Mg, and PA6, and 176 μm for PA6 Black. According to SI_{dens} index, powder spreadability increases as the spread layer density approaches the powder bulk density, which is assumed to represent the maximum layer density. Bulk densities of Table 1, measured with FT4 and GeoPyc, were used as reference bulk densities to evaluate this index. Under heavy compaction, bulk densities may exceed the reference values used, but this is unlikely with a spreading process as the one tested. Therefore, it can be assumed that also SI_{dens} ranges between 0 and 1, and it increases with layer quality in terms of density.

3. Results

3.1. Flow properties comparison

All powder materials were tested for powder flowability by shear testing. Several papers in the literature have proven a limited relevance of Powder flowability to powder spreadability [13,15], which is likely to be due to the different characteristics of the controlled powder shear in shear testing and the complex powder dynamics occurring in the powder spreading process. Nevertheless, shear testing provides bulk parameters which are used to discuss some of the spreading results obtained in this work. Bulk properties and powder flowability obtained with shear testing depend on many particle and powder properties combined (e.g. particle size, PSD, particle shape, interparticle forces, particle surface quality, etc.), and differences or similarities in bulk properties may depend on such combinations.

The flow functions of all powders, plotted in Fig. 3, indicate that for the reported range of σ_1, all are free-flowing powders according to the Jenike classification [42]. Except for AlSi10Mg and PA6 Black, at σ_1 of 1837 Pa and 2009 Pa, respectively, the powders' flow functions fall into the transition region between the easy flowing and free flowing regimes.

C and σ_1 were measured at different pre-shear conditions [43] and reported in Table 2, with respective unconfined yield strength, f_c, static angle of internal friction, Φ_i, and dynamic angle of internal friction, Φ_e. In order to assess the C in conditions similar to the spreading flow regime of the first layer, σ_1 was calculated assuming dynamic conditions of a heap of powder sliding on the underlying base and named as C_s. For the calculation, the normal stress, σ_n, was assumed to be equal to the hydrostatic pressure of the pile $P = \rho g h$, where ρ is the bulk density of the powder reported in Table 1 and h is the average height of the pile during the experiments, set at about 0.015 m. The dynamic angle of internal friction, Φ_e, reported in Table 2, was employed to identify the Mohr circle representing the stress status of the sliding heap. The major principal stress σ_1 was calculated from the Mohr circle and its relative C was calculated from the regression line of C versus σ_1.

The adhesion, τ_{ad}, and wall friction angles, Φ_w, were determined from the wall yield loci and are reported in Table 3. In order to assess the adhesion τ_{ad} at stress conditions similar to the spreading flow regime of the first powder layer, the adhesion was calculated at σ equal to the hydrostatic pressure of the heap and named as τ_{ad_s}.

For each powder, the extrapolated adhesion and cohesion values were compared to examine the balance between two competing behaviours during spreading. Adhesion reflects the tendency of the powder to remain attached to the spreading surface, representing the limiting shear stress that keeps the powder attached to a surface at very low normal stresses, as it occurs in the spreading process. Cohesion, instead, is the internal shear stress, also at very low normal stresses, generated by powder shear, as it occurs within the powder just in front of the moving blade. It can be hypothesised that lower values of the cohesion to adhesion ratio should be related to better spreading behaviour under process conditions. Results on the cohesion and adhesion of powders,

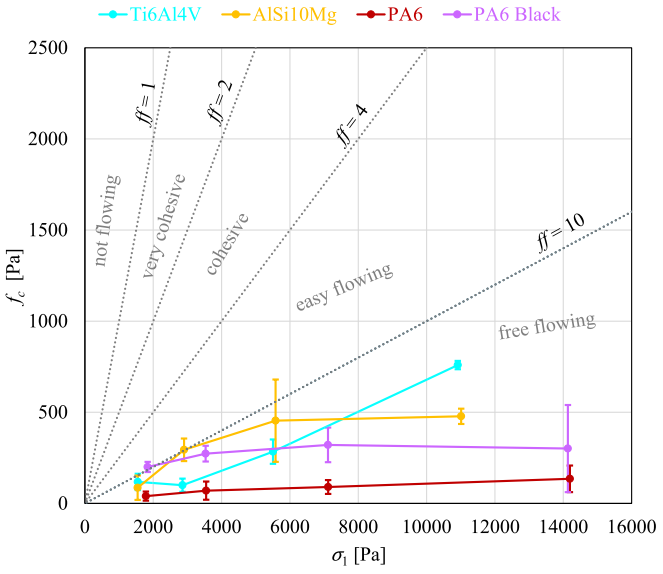


Fig. 3. Flow functions of Ti6Al4V, AlSi10Mg, PA6, and PA6 Black, calculated at pre-shear normal stresses equal to 1, 2, 4, and 8 kPa.

Table 2
Internal shear testing results for Ti6Al4V, AlSi10Mg, PA6, and PA6 Black.

Material	Yield Loci	σ_1 [Pa]	f_c [Pa]	C [Pa]	Φ_i [°]	Φ_e [°]
Ti6Al4V	1	1549	47	14	30.1	31.3
	2	2856	94	26	31.4	32.6
	3	5504	259	72	31.6	32.8
	4	10,913	663	194	29.2	32.1
AlSi10Mg	1	1544	29	8	31.0	30.5
	2	2902	266	76	30.3	32.2
	3	5581	353	99	31.4	32.7
	4	11,012	283	79	31.8	30.6
PA6	2	1786	40	7	36.7	38.7
	3	3549	70	9	36.6	37.2
	4	7119	90	12	35.5	35.8
	5	14,194	135	16	35.7	35.7
PA6 Black	1	1837	200	50	36.8	39.4
	2	3533	273	68	36.9	38.7
	3	7115	321	81	36.6	37.7
	4	14,135	301	85	36.5	37.0

Table 3
Wall shear testing results for Ti6Al4V, AlSi10Mg, PA6, and PA6 Black.

	τ_{ad} [Pa]	Φ_w [°]
Ti6Al4V	−16.32	18.9
AlSi10Mg	13.68	17.9
PA6	10.21	25.8
PA6 Black	63.72	20.8

extrapolated at zero consolidation stress to be relevant to the spreading process, are reported in Table 4 together with their ratio. Inspection of the Table shows that in every case adhesion is larger than cohesion.

Also, the effective angle of internal friction, is an interesting parameter for the spreading process as it is an indirect measure of the resistance to steady shear flow of the powder in which frictional and cohesive interparticle forces are effectively combined and, for prevailing friction as for the free-flowing material tested, generally it is not much dependent on the consolidation stress and it is not much different from the internal friction angle. The values reported in Table 2 confirm this hypothesis. In contrast, the larger values of Φ_i and Φ_e found for the two polymers are likely to be mostly attributed to the lower sphericity of the particles of these materials. Extrapolated values at zero consolidation are also reported in Table 4.

3.2. Spreading experiment conditions

The testing conditions could not be fully controlled during the experimental campaign. However, room temperature and relative humidity were recorded at the beginning and end of each test and reported in the Supplementary Material. These measurements provide context for any day-to-day variability. Inspection of the recorded values indicates that temperatures remained stable across all materials, near 21–22 °C with negligible drift between the start and end readings. Also, relative humidity changed slightly within each test run: metals and PA6 operated mostly in the 28–36% RH range, while PA6 Black was tested at a higher, steady humidity near 44–45%. The observed variations in temperature and relative humidity were small enough to be considered unlikely to introduce substantial bias in comparisons between tests performed with the same powder for the metals and PA6 Black. However, because PA6 is highly hygroscopic, even the observed humidity variations may have affected its behaviour.

Table 4
Normal stress and major principal stress at low load conditions, dynamic angle of internal friction, powder cohesion and adhesion with aluminium contact wall at room temperature, calculated at stress status similar to spreading flow regime of the first powder layer, and their ratio.

	σ_n [Pa]	σ_1 [Pa]	Φ_e [°]	τ_{ad_s} [Pa]	C_s [Pa]	C_s/τ_{ad_s} [−]
Ti6Al4V	357.57	765.48	32.00	106.37	6.81	0.064
AlSi10Mg	204.39	428.04	31.77	79.63	0.99	0.012
PA6	77.25	191.99	38.27	47.60	5.19	0.11
PA6 Black	101.53	254.99	39.44	102.22	33.211	0.32

3.3. Acquisitions and apparent quality

Fig. 4 to Fig. 7 show the images (panes a and b), profilometer scans (panes c and d), pixel intensity distribution of images (pane e), height distribution of scanning (pane f), and power spectra comparison (pane g) of the layers obtained for Ti6Al4V, AlSi10Mg, PA6, and PA6 Black at a spreading speed of 50 mm/s, the lowest spreading speed tested. The images were captured without flat-field correction and grey-level normalisation. The aperture was 4.1 for every acquisition, while the ISO was automatically set to 100 for polymeric powders and to 400 for metal powders. Camera exposure was varied, with 0.25 s for PA6, 2.5 s for PA6 Black, 0.01 s for Ti6Al4V, and 0.0125 s for AlSi10Mg. White balance was low and negligible considering the mainly monochromatic acquisitions. In Fig. 4 to Fig. 7, 2-D representations of profilometer scans are images in grey scale in which the grey level is proportional to the local height detected by the profilometer. In order to account for the different bin dimensions 19.0 μm × 14.1 μm ($x \times y$), to be compared with photographic images, these plotted images were stretched in the x direction by a factor 19.0/14.1 and resized in order to match the same length as the photographic images. The stretching procedure is finalised only for the 2D representation of the surface scan. It does not affect the data processing described above in Section 2.2.4, where it appears that only pixel and bin size in the x direction are relevant and, when necessary, were appropriately used with their real values.

Comparing the photographic images and the scanning representation, some differences between them are caused by the different nature of the acquisition. While the camera image relies on the shadows created by the grazing illumination in the spreading direction, the laser profilometer measures local bed heights. Therefore, the photographic images tend to highlight height variations in the spreading direction, detecting as bright areas the downward slopes in the spreading direction and as darker areas the upward slopes in the spreading direction. Surface scans instead represent as bright areas the peaks and as darker areas the valleys without any preferential direction, which may explain, together with the different pixel resolution, the slightly larger granularity of the scanned height images than the grazing light photographic images. The differences associated with grey levels in the two different image representations are visible in the grey level distribution plotted in Fig. 4 to Fig. 7, in panes e) for the grazing light images and panes f) for the scanned height images. The former are generally asymmetric due to the complex interaction between grazing light and surface roughness to produce shadows, in spite of quite symmetrical distributions of local surface height detected by the laser scan technique.

Inspection of Fig. 4 to Fig. 7 indicates that the metal powders in Fig. 4 and Fig. 5 provide smoother surfaces than the polymer powders in Fig. 6 and Fig. 7. In particular, the Ti6Al4V powder showed the smoothest spread layer. Inspection of the enlarged portion of the surface representations reported in panes b and d of Fig. 4 to Fig. 7 reveals that some large agglomerates are visible for PA6 and PA6 Black. In contrast, the two metal powders show only small, compact agglomerates composed of a few particles. Despite the significant difference in resolution between images acquired under grazing illumination and profilometer scans, all results indicate that polymers exhibit larger surface textures than metals. The much larger density of the metal particles, combined with slightly better flow properties of the same materials discussed above in Section 3.1 can justify a better ability of the metal powder to settle and explain differences between the surface quality of metal and polymeric powders [44].

The images and scans obtained at all the other spreading speeds investigated are shown in the Supplementary Material. At 75 mm/s,

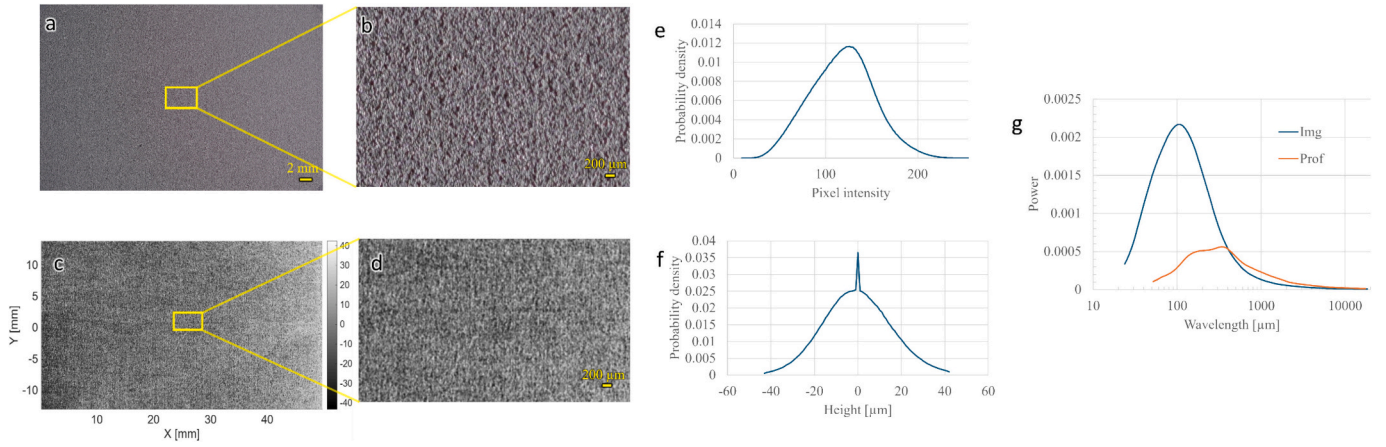


Fig. 4. Surface of the layer obtained by spreading Ti6Al4V at 50 mm/s: a) photographic image obtained with grazing light, yellow rectangle indicates the magnified area; b) detail of nine times magnification of the photographic image; c) scanning profile map, yellow rectangle indicates the magnified area; d) detail of the nine times magnification of the scanning profile map; e) pixel intensity probability density of greyscale image; f) height probability density of profile scanning; and g) powder spectra from image analysis and profile scanning. (For interpretation of the references to colour in this figure legend, the reader is referred to the web version of this article.)

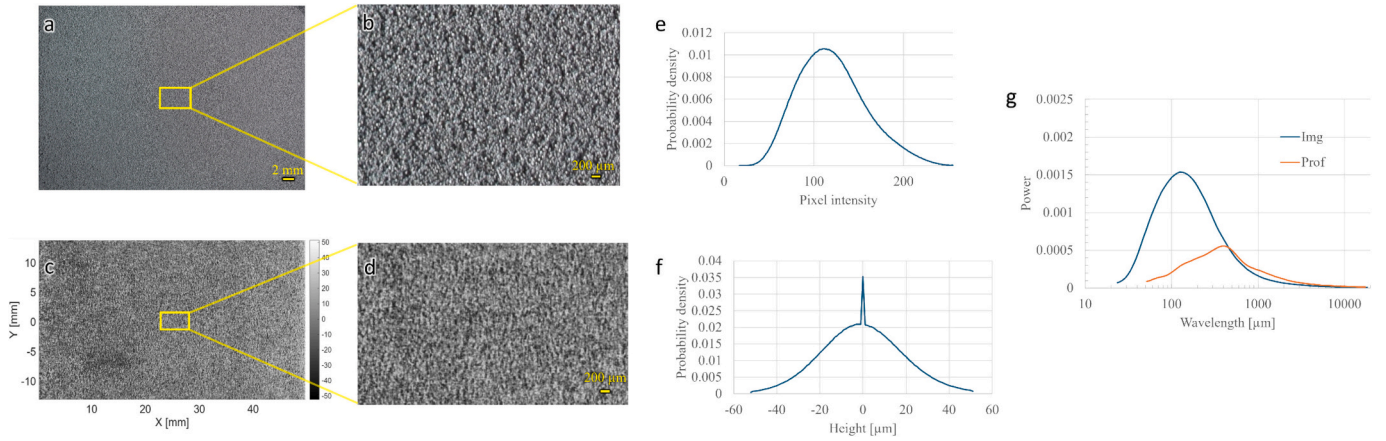


Fig. 5. Surface of the layer obtained by spreading AlSi10Mg at 50 mm/s: a) photographic image obtained with grazing light, yellow rectangle indicates the magnified area; b) detail of nine times magnification of the photographic image; c) scanning profile map, yellow rectangle indicates the magnified area; d) detail of the nine times magnification of the scanning profile map; e) pixel intensity probability density of greyscale image; f) height probability density of profile scanning; and g) powder spectra from image analysis and profile scanning. (For interpretation of the references to colour in this figure legend, the reader is referred to the web version of this article.)

there are only slight differences with the 50 mm/s results, except for Ti6Al4V, where the surface appears noticeably rougher. At 100 mm/s, visible stripe-shaped irregularities appear on the Ti6Al4V layer, running perpendicular to the spreading direction. These stripe patterns are also faintly visible for PA6 and AlSi10Mg. For PA6 Black, instead, some unfilled spots are clearly visible at the highest spreading speed tested. The vertical-stripe pattern can be attributed to elevated powder moisture, driven by the ambient relative humidity. A previous study reported the same pattern of vertical stripes. It showed that fine powders are highly sensitive to moisture: at higher moisture levels, spreading produced stripe-like surface irregularities that degraded the quality of the final 3D part [45]. Further studies are needed to assess the causes of the vertical stripes that may possibly depend on slip-stick phenomena in the powder shearing induced by the blade edge or on the avalanching of powders in the powder heap in front of the blade.

3.4. Power spectra analysis

Wavelet transforms were applied to images acquired under grazing illumination and to 3D profilometer scans, yielding an image-based and a scan-based power spectrum for each test. The power spectra of the tested materials at 50 mm/s are shown in panels g of Fig. 4 to Fig. 7. The metal powders exhibited multimodal spectra within the range of the unimodal peak of the power spectra obtained by image analysis. Also, polymer powders showed multimodal spectra with less clearly defined peaks, and the maximum peak still fell within the same wavelength range as the prevailing wavelengths identified by the image analysis. The characteristic wavelength was then taken as the dominant peak in each spectrum, even when multiple peaks were present. The main peak is relative to the most relevant pattern present on the layer surface. It was considered a representation of the average dimension of the most present agglomerates and flaws. This assumption was corroborated by validations, where an image analysis software tool (ImageJ, V 1.54, National Institutes of Health, Bethesda, MD, USA) was employed to manually measure a subset of the visible agglomerates, revealing dimensions in the same order of magnitude as the power spectrum peak wavelength. The positions of the maximum peaks differed between the image and laser-scan power spectra.

Fig. 8 shows power spectra for Ti6Al4V at different spreading speeds, with each panel comparing the image-based and profilometer-based

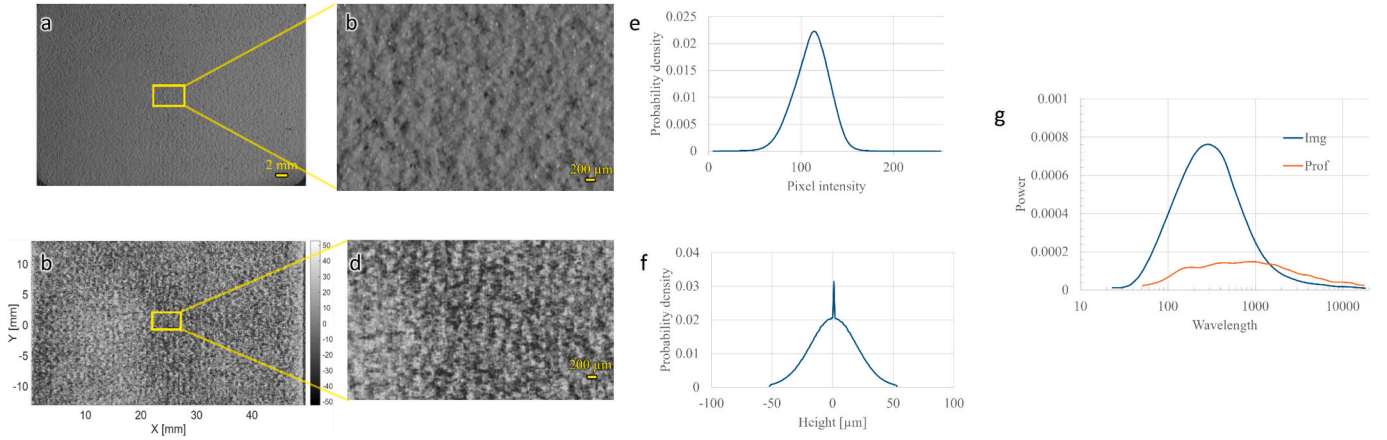


Fig. 6. Surface of the layer obtained by spreading PA6 at 50 mm/s: a) photographic image obtained with grazing light, yellow rectangle indicates the magnified area; b) detail of nine times magnification of the photographic image; c) scanning profile map, yellow rectangle indicates the magnified area; d) detail of the nine times magnification of the scanning profile map; e) pixel intensity probability density of greyscale image; f) height probability density of profile scanning; and g) powder spectra from image analysis and profile scanning. (For interpretation of the references to colour in this figure legend, the reader is referred to the web version of this article.)

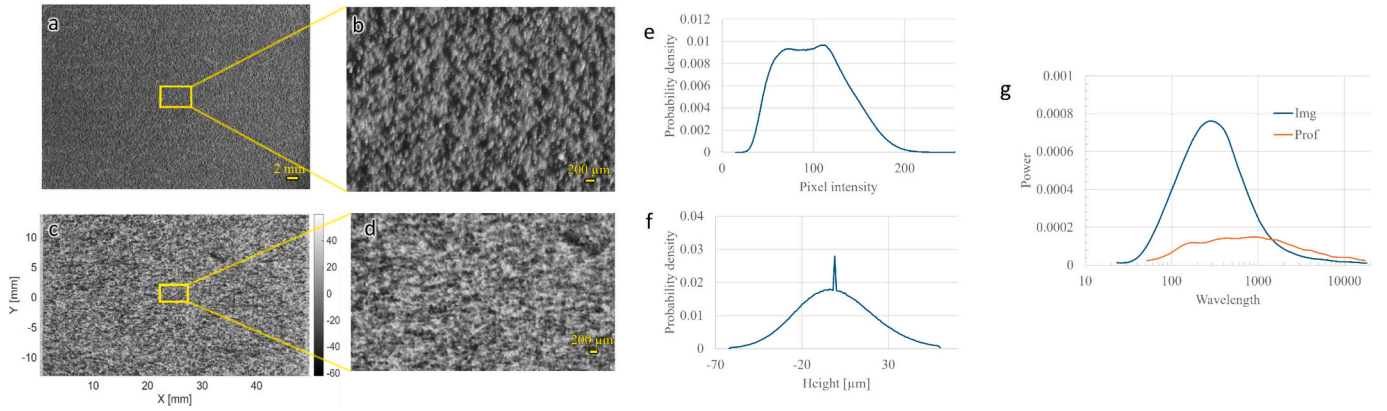


Fig. 7. Surface of the layer obtained by spreading PA6 Black at 50 mm/s: a) photographic image obtained with grazing light, yellow rectangle indicates the magnified area; b) detail of nine times magnification of the photographic image; c) scanning profile map, yellow rectangle indicates the magnified area; d) detail of the nine times magnification of the scanning profile map; e) pixel intensity probability density of greyscale image; f) height probability density of profile scanning; and g) powder spectra from image analysis and profile scanning. (For interpretation of the references to colour in this figure legend, the reader is referred to the web version of this article.)

spectra. Corresponding plots for the other materials are provided in the Supplementary Material. In Fig. 8, every spectrum shows a peak around 140 µm, which is related to the combination of the profilometer's acquisition rate and bed advancement speed.

Differences in peak positions in wavelet power spectra from image analysis and scanning profiles may depend on the different abilities of these two procedures to describe surface shapes. Indeed, surface scanning acquires the height values of surface positions, allowing for different z positions of subsequent peaks or valleys. Instead, image analysis does not distinguish the heights of subsequent peaks or valleys, assigning them similar pixel intensities. Therefore, the wavelet peaks shown in the profilometry powder spectrum weigh the distances between subsequent peaks and valleys by their intensity; on the other hand, in image analysis, shade intensity is not directly related to the height of peaks and valleys but depends mostly on the length of the shadows projected from particles and agglomerates. Such differences might justify the broader peaks in the wavelet power spectrum obtained with profilometry, which can be considered to reflect a wider range of height wavelengths describing the surface profile than the light intensity fluctuations detected in an image. Even if derived from a less detailed characterisation of the surface, it should be recognised that in principle profilometry power spectra have a more direct physical meaning than image-based power spectra. Nevertheless, both procedures will be further considered as the purpose of this work is to understand the feasibility of different methods to provide information relevant to the understanding of the layer quality, also in view of on-line process application, for which the image-based analysis is undoubtedly easier to apply.

The average peak wavelength measured for all materials at each spreading speed is reported in Table 5. For multimodal spectra, only the highest peak was considered.

It is reasonable to hypothesise that the characteristic wavelengths in the spectra reflect the size of clusters and agglomerates formed during spreading, given the particle sizes and the samples analysed. However, the prevailing wavelengths obtained from image-based and profilometer analyses often differ, likely due to the above hypothesised reasons. These differences propagate to the *SI*, producing noticeable discrepancies even under similar spreading conditions (included in Table 5). This effect is most pronounced in bimodal spectra with similar peak intensities. Under these conditions, the peaks occur at comparable wavelengths, but the dominant peak may vary from one test to another.

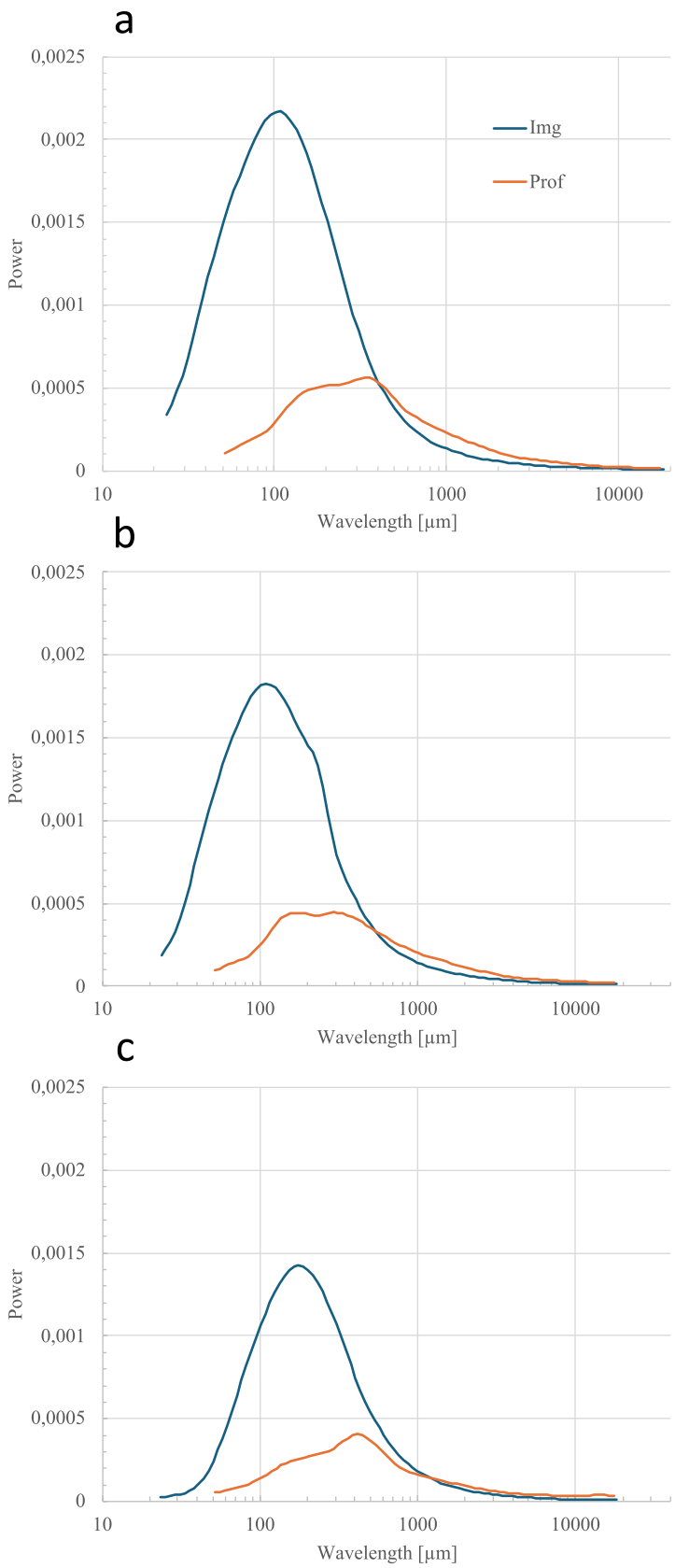


Fig. 8. Power spectra obtained from image analysis (in blue) and profilometer analysis (in red) of Ti6Al4V powder at: a) 50 mm/s; b) 75 mm/s; c)100 mm/s. (For interpretation of the references to colour in this figure legend, the reader is referred to the web version of this article.)

Table 5
Wavelet power spectra peak wavelength (PW), profilometry roughness values S_a, skewness values S_{sk}, kurtosis values S_{ku}, greyscale images roughness values G_a, skewness values G_{sk}, kurtosis values G_{ku}, spreadability indexes, and Inertia number for the different materials spread at different speeds.

		Spreading speed		
Material		50 mm/s	75 mm/s	100 mm/s
Ti6Al4V	Image PW, μm	111.3 ± 4.6	125.4 ± 15.6	119.1 ± 4.6
	Profilometry PW, μm	231.9 ± 90.5	265.1 ± 87.0	335.0 ± 0.7
	S_a, μm	14.8 ± 0.8	15.7 ± 0.9	16.1 ± 1.6
	S_{sk}	−0.025 ± 0.042	−0.003 ± 0.020	−0.063 ± 0.026
	S_{ku}	2.81 ± 0.02	2.77 ± 0.02	2.78 ± 0.01
	G_a	26.8 ± 1.1	24.4 ± 4.3	25.6 ± 1.2
	G_{sk}	0.027 ± 0.037	0.111 ± 0.165	−0.062 ± 0.079
	G_{ku}	2.82 ± 0.03	3.02 ± 0.37	2.95 ± 0.09
	SI_{img}	0.297 ± 0.012	0.266 ± 0.031	0.277 ± 0.01
	SI_{prof}	0.155 ± 0.05	0.136 ± 0.05	0.0985 ± 0.00022
	SI_{dens}	0.66 ± 0.07	0.68 ± 0.03	0.66 ± 0.03
	I	0.28	0.43	0.57
AlSi10Mg	Image PW, μm	140.0 ± 5.4	146.4 ± 5.7	172.7 ± 18.1
	Profilometry PW, μm	413.0 ± 0	413.0 ± 0	413.0 ± 0
	S_a, μm	18.6 ± 0.6	19.7 ± 0.4	21.0 ± 1.4
	S_{sk}	0.025 ± 0.022	0.001 ± 0.021	0.043 ± 0.031
	S_{ku}	2.79 ± 0.02	2.80 ± 0.01	2.77 ± 0.02
	G_a	32.0 ± 1.5	32.6 ± 0.9	28.5 ± 2.5
	G_{sk}	0.486 ± 0.040	0.418 ± 0.077	0.270 ± 0.067
	G_{ku}	2.90 ± 0.06	2.79 ± 0.05	3.02 ± 0.07
	SI_{img}	0.29 ± 0.01	0.27 ± 0.01	0.23 ± 0.03
	SI_{prof}	0.10 ± 0	0.10 ± 0	0.10 ± 0
	SI_{dens}	0.72 ± 0.06	0.63 ± 0.06	0.55 ± 0.02
	I	0.34	0.52	0.69
PA6	Image PW, μm	370.7 ± 25.7	398.4 ± 28.1	397.4 ± 27.7
	Profilometry PW, μm	950.3 ± 65.8	953.2 ± 110.2	950.3 ± 65.8
	S_a, μm	20.7 ± 1.7	20.9 ± 0.6	19.7 ± 1.2
	S_{sk}	−0.036 ± 0.026	−0.010 ± 0.025	−0.043 ± 0.044
	S_{ku}	2.78 ± 0.01	2.79 ± 0.02	2.79 ± 0.02
	G_a	14.9 ± 2.0	17.3 ± 1.1	15.3 ± 2.3
	G_{sk}	−0.457 ± 0.135	−0.647 ± 0.066	−0.439 ± 0.219
	G_{ku}	3.68 ± 0.13	3.57 ± 0.21	3.65 ± 0.45
	SI_{img}	0.12 ± 0.01	0.12 ± 0.01	0.12 ± 0.01
	SI_{prof}	0.05 ± 0	0.04 ± 0.01	0.05 ± 0
	SI_{dens}	0.43 ± 0.04	0.37 ± 0.02	0.43 ± 0.06
	I	0.40	0.59	0.79
PA6 Black	Image PW, μm	310.9 ± 13.1	330.2 ± 68.5	349.5 ± 42.7
	Profilometry PW, μm	907.8 ± 70.9	1142.0 ± 45.2	1001.9 ± 152.4
	S_a, μm	20.0 ± 0.1	20.1 ± 0.3	20.7 ± 1.4
	S_{sk}	0.105 ± 0.011	0.099 ± 0.007	0.087 ± 0.010
	S_{ku}	2.76 ± 0.02	2.76 ± 0.01	2.77 ± 0.02
	G_a	26.6 ± 2.6	27.3 ± 3.3	20.8 ± 4.6
	G_{sk}	0.155 ± 0.111	0.255 ± 0.201	0.027 ± 0.130
	G_{ku}	2.44 ± 0.10	2.47 ± 0.05	2.61 ± 0.15
	SI_{img}	0.24 ± 0.01	0.23 ± 0.05	0.21 ± 0.02
	SI_{prof}	0.08 ± 0.01	0.06 ± 0	0.08 ± 0.01
	SI_{dens}	0.36 ± 0.01	0.36 ± 0.01	0.35 ± 0.01
	I	0.51	0.76	1.01

3.5. Roughness-based results

The scans mentioned in Section 3.3 were analysed, and the S_a was calculated. Table 5 reports the average surface roughness expressed in μm, calculated from all the experiments performed. Comparison of S_a values between different materials confirms the qualitative observation of the surface images, and indicates that the heavier metals, Ti6Al4V in particular, tend to generate smoother surfaces driven by the settling effect of the weight not balanced by similar changes of the surface interparticle forces indirectly estimated by equivalent bulk flowability. On the other hand, based on data in Table 5, using 50 mm/s as the baseline, roughness S_a rises with the spreading speed for metal powders, indicating that faster spreading generally yields a rougher spread powder layer. From 50 to 100 mm/s, roughness increases of about 9% for Ti6Al4V and 13% for AlSi10Mg. Polymeric powders, instead, do not show significant changes in roughness, just a small increase of ~4% for PA6 Black. In this case, the different dependence on spreading speed between polymeric and metal powders may be related to the increasing importance of particle momentum as spreading speed increases, while cohesive interparticle forces remain unchanged. Cohesive forces limit relative particle motion, whereas the greater mass of the metal particles may increase their momentum and promote more independent and less uniform settling after blade passage [46]. Standard deviations tend to increase with the spreading speed for most powders, indicating higher run-to-run variability at faster spreading speeds.

Regarding the raw results of S_a, reported in Table 5, it should be recognised that the average particle size and the width of PSDs may affect powder roughness and produce larger S_a, as the displacement of single particles or groups of a similar number of particles on the surface may produce different changes in the surface height. For this reason, to compare results of different powders characterised by different particle sizes, the indices derived from the image- and profilometer-analyses are normalised on d_{50}, which represents a characteristic parameter of powders' PSD, reducing the effect of particle dimensions on the results.

Previous studies support the same overall trend. Yim et al. [47] reported an increase in roughness for metal powders as the spreading speed increased from 50 to 200 mm/s. Sillani et al. [48] observed a similar increase in roughness between 50 and 200 mm/s for eight polymer powders. In the present work, the smaller changes may be related to the narrower speed range investigated. In addition, the results may have been influenced by powder hygroscopicity and by sensitivity to small variations in moisture content [49].

3.6. Density-based results

Bulk density values for all powders are listed in Table 1. To measure the powder layer density, the weight of the spread powder and the volume of the tray were recorded. The powder weight was measured using an analytical scale. The volume was considered uniform and calculated as the pocket surface area multiplied by the distance between the blade edge and the bottom of the pocket. The density-based results are expressed using the SI_{dens}, defined in Eq. (8). Results are presented in Table 5.

The results showed that Ti6Al4V had the highest layer SI_{dens}, followed by AlSi10Mg, PA6 Black, and finally PA6. Ti6Al4V was also less affected by increasing spreading speedcompared to the other powders. Higher SI_{dens} values for heavier material confirm the positive effect of the particle density on compact and more regular settling of particles [44]. In this case, also the particle size, which is larger for powders with lower indices, may have a role. In fact, the distance left between the surface of the generated layer and the edge of the blade is intrinsically related to the particle size. It should increase with it, defining a worse layer filling capacity by powders with larger particles.

3.7. Inertial number

The effect of spreading speed can also be analysed using the inertial number [50], I, which can be associated with the spreading process and is defined as follows:

$$I = \frac{\dot{\gamma} d}{\sqrt{P/\rho}} \tag{10}$$

Where the shear rate, $\dot{\gamma}$, can be defined as the ratio between the spreading speed v and the allowed gap h:

$$\dot{\gamma} = \frac{v}{h} \tag{11}$$

d and ρ are the particle size and density, and P is the vertical stress (hydrostatic pressure) applied to the forming layer. Results indicate that higher I are associated with poorer layer quality, more jamming phenomena, larger agglomerates, higher roughness, and lower layer density [18,51]. To analyse results in terms of I, Eq. (10) can be rearranged as

$$I = \frac{\dot{\gamma} d_{50}}{\sqrt{P/\rho_p}} \tag{12}$$

Shear rate, $\dot{\gamma}$, can be defined as:

$$\dot{\gamma} = \frac{v}{\delta + w} \tag{13}$$

where v is the spreading speed, and $\delta + w$ is the distance between the blade and the bottom of the pocket bed. d_{50} and ρ_p are the median particle size and density. Combination of (12) and (13) leads to the following:

$$I = \left(\frac{d_{50} \sqrt{\frac{\rho_p}{P}}}{\delta + w} \right) v \tag{14}$$

During the experiments, it was not possible to directly measure the hydrostatic pressure P or the shear stress during spreading. However, it is known that the pressure and shear stress acting on particles in the gap are quite low—typically in the range of a few hundred Pascals [15,18]. These stress levels can vary depending on the mechanical properties of the powder, such as its stiffness or resistance to deformation. Table 5 shows the approximated inertial number for each powder and spreading speed, assuming that the hydrostatic pressure $P = \rho_p \cdot g \cdot (\delta + w)$. This latter assumption, tend to somewhat underestimate the results obtained in DEM simulations of similar systems that show the occurrence of force chains between the blade and the layer bottom [52]. Still, it is reasonably of the same order of magnitude. Also, it makes the inertial number independent of the particle density, which cancels out in the ratio under the square root in Eq. (14), making the inertia number dependent, in our tests, only on the particle size and on the blade velocity. PA6 Black exhibited higher$I$, because of the larger d_{50} with respect to the other powders.

The results reported in Table 5 highlight that, I increases with spreading speed for every powder. However, the spreadability indices do not decrease proportionally with I, and the ranking of the materials according to I does not consistently coincide with the ranking obtained from the spreadability indices. PA6 Black had the highest calculated I and showed unfilled areas at high spreading speed, whereas Ti6Al4V developed visible vertical stripe patterns despite having the lowest calculated I among the tested powders at the same spreading speed. These observations indicate that the adopted definition of I captures the effects of spreading speed and particle size but does not fully describe the spreading behaviour. The assumed hydrostatic pressure may also be underestimated because the additional normal stress generated beneath the blade is neglected. Moreover, cohesion and adhesion are not included in the classical formulation of I. For fine particles, these forces may oppose inertia-driven rearrangement and therefore limit the ability of I alone to represent the spreading behaviour. Specific tests should be carried out to evaluate these effects, which go beyond the purpose of the present work.

3.8. Indices comparison

Based on the calculated indices reported in Table 5, it is difficult to identify a direct relationship among the indices obtained under the same experimental conditions. Although most of the indices suggest better spreadability for the metal powders, they do not provide a single and fully consistent ranking of the materials. This is expected because each index describes a different feature of the spread layer. Some indices are more sensitive to density, whereas others are more related to surface characteristics. It can be noted that powders made of denser particles showed a more pronounced change in the density index with spreading speed. At higher speeds, the greater particle mass of the metal powders may enhance momentum effects and alter the amount of material retained in the pocket. Accordingly, the layer mass changed more for the metal powders than for the polymeric powders, which were less dense and already showed poorer packing at lower spreading speeds. On the other hand, the image analysis was able to capture the changes in the layer surface but was not able to correlate with the overall packing of the layer. Unfortunately, the profilometer analysis suffered from poor resolution due to the device, leading to very similar indices inadequate for classification. For this reason, a combined approach based on both density-related and surface-related metrics is recommended to achieve a more complete and reliable evaluation of spreading performance. The layer density analysis combined with image analysis can be an adequate solution to collect both packing, density and surface information. On the other hand, the proposed image analysis method is affected by lighting and camera positioning. Introducing different angles for the lighting and positioning the light source in different sides of the layer may result in more complete results. The topography analysis may be a good alternative to image analysis. Still, it is challenging to combine an adequate resolution of the device, non-intrusivity, and a sample large enough to be representative of the entirety of the powder layer. Moreover, it would be impractical to perform in a single analysis both surface and density assessment. However, the combination of two parallel methods, one for density and one for surface assessment, would provide a more comprehensive evaluation of the spread layer. It would also be suggested that the selected methods guarantee the analysis of the same portion of the layer, similarly to the aforementioned analysis techniques.

Fig. 9 compares all indices across materials and conditions and shows a common trend: surface quality and layer density decline as spreading speed increases, consistent with previous studies [47,48]. Every spreadability index decreases with speed for Ti6Al4V. A similar result was showed for AlSi10Mg in every index but Si_{prof} which showed negligible variations. Polymeric powders (PA6 and PA6 Black) follow this trend within the error bars, although its mean at the highest speed appears shifted; given PA6's strong hygroscopicity and sensitivity to small changes in temperature and humidity [28,53], this variability is expected and does not contradict the trend.

3.9. Indices statistics

The Pearson correlation analysis was performed on the indices to evaluate their mutual statistical relationship, including the analysis controlling for the spreading speed. The analysis results are reported in Table 6. Pearson correlation analysis revealed that the relationships among the three spreadability indices were strongly material dependent. For Ti6Al4V, no significant pairwise correlation was initially observed, although SI_{dens} and SI_{prof} showed a relatively strong positive association ($r = 0.620$). After controlling for spreading speed, this relationship increased to $r = 0.739$ and became statistically significant $p = 0.036$, suggesting that the different sensitivity of the indices to the process condition may partially obscure their agreement. A different behaviour

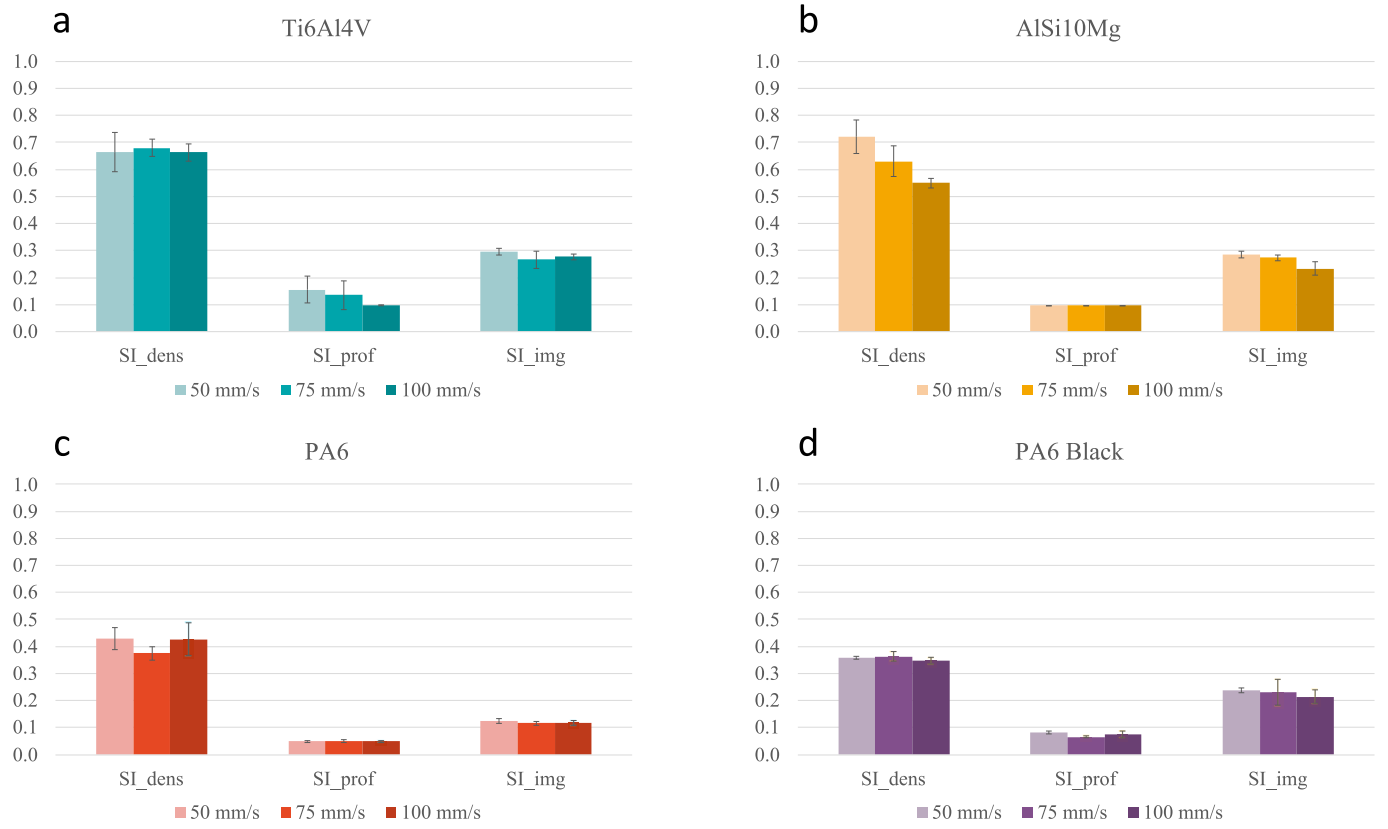


Fig. 9. Indices comparison at increasing spreading speeds for: a Ti6Al4V, b AlSi10Mg, c PA6, and d PA6 Black.

Table 6
Statistical analysis on the indices correlation evaluating Pearson r and p value, assessing the influence of spreading speed on the relationship by introducing the same parameters calculated by controlling spreading speed.

Material	Indices	Pearson r	p	Partial $r_{\|v}$	$p_{\|v}$
Ti6Al4V	$SI_{dens} - SI_{prof}$	0.620	0.075	0.739	0.036
	$SI_{dens} - SI_{img}$	0.084	0.829	0.088	0.837
	$SI_{prof} - SI_{img}$	0.377	0.317	0.215	0.609
AlSi10Mg	$SI_{dens} - SI_{prof}$	n.a.	n.a.	n.a.	n.a.
	$SI_{dens} - SI_{img}$	0.713	0.031	0.024	0.956
	$SI_{prof} - SI_{img}$	n.a.	n.a.	n.a.	n.a.
PA6	$SI_{dens} - SI_{prof}$	−0.577	0.104	−0.577	0.134
	$SI_{dens} - SI_{img}$	0.783	0.012	0.862	0.006
	$SI_{prof} - SI_{img}$	−0.574	0.106	−0.635	0.091
PA6 Black	$SI_{dens} - SI_{prof}$	−0.263	0.495	−0.399	0.328
	$SI_{dens} - SI_{img}$	0.896	0.001	0.882	0.004
	$SI_{prof} - SI_{img}$	−0.086	0.826	−0.210	0.618

was observed for AlSi10Mg. SI_{dens} and SI_{img} were significantly correlated, with $r = 0.713$ and $p = 0.031$, but both indices also showed strong negative correlations with spreading speed, with $r = -0.867$ and -0.814, respectively. Accordingly, their partial correlation became negligible after controlling for speed showing $r = 0.024$, indicating that their apparent agreement was predominantly associated with their common response to the spreading speed.

Conversely, a strong and speed-independent agreement between SI_{dens} and SI_{img} was observed for both polymeric powders. For PA6, their correlation increased from $r = 0.783$ to a partial correlation of $r = 0.862$, whereas PA6 Black showed similarly high coefficients before and after controlling for speed, with $r = 0.896$ and 0.882, respectively. No statistically significant correlation with spreading speed was detected for either polymer. Overall, these results indicate that the different spreadability indices cannot be regarded as interchangeable measures of powder-bed quality. Their agreement, as well as their sensitivity to spreading speed, depends on the investigated material and on the physical feature of the deposited layer captured by each measurement technique.

4. Discussion

Measured flow properties indicated that both metal and polymeric materials are free-flowing powders. These powders also exhibited high overall spreadability and are characterised by wall adhesion to the aluminium surface that exceeded internal cohesion. These results also suggest a higher tendency for the powder to adhere to the contact surface rather than agglomerating in front of the blade and can explain the limited tendency of the material tested to produce long linear flaws in the spreading direction.

Powder flowability results between the materials tested suggested a concurrent effect of the effective shear forces indicated by the effective angle of internal friction and of the gravity forces, related to the particle density, favouring metal over polymers. Visual inspection showed that metal powders possessed lower apparent surface roughness and higher sphericity than polymer powders, which may explain the reduced internal friction. However, S_a limitedly changed during the testing of polymer powders. For powder layers, S_a primarily depends on the particle arrangement and their relative positioning, particularly of particles in the upper layer. Metal powders, being more spherical, having a lower effective angle of internal friction, and containing denser particles with a lower interparticle-force-to-weight ratio than the polymeric powders (Fig. 1), tend to form smoother surfaces. Their greater particle mass may also make S_a more sensitive to spreading speed through momentum effects.

Power spectra derived from images were predominantly unimodal, whereas profilometer spectra were frequently multimodal. This divergence reflects the fundamental nature of the data acquisition methods. In image analysis under grazing light, pixel intensities serve as wavelet

inputs, where bright regions are downward slopes and dark regions are upward slopes. Profilometry, instead, records absolute heights, so it is more sensitive to the actual amplitudes of peaks and valleys. Furthermore, while image analysis under grazing light offers superior in-plane resolution, laser profilometry provides height profiles valid also in the *y* direction, which, however, were not used in this work; the specific impact of resolution is further detailed in Appendix A. Despite these differences, every test showed that the profilometer and image spectra shared at least one peak within a similar wavelength band and a comparable spectral range. This result indicates that both methods capture the fundamental spacing between peaks and valleys. However, results also show that image power spectra tend to shift the prevailing wavelengths towards lower values than profile power spectra, indicating that the grazing light may produce similar grey level intensities for large and small changes of the bed height and, thereby, enhancing the role of the shorter wavelengths in the wavelength distribution.

Additionally, each method possesses inherent constraints. Profilometry may be hindered by the available resolution and powder's reflectivity. On the other hand, image analysis may be sensitive to lighting angle; suboptimal illumination may fail to produce satisfactory shadows or contours necessary to detect the flaws caused by z-position differences or light propagating parallel to the features. The high reflectivity of polished metal surfaces may produce single particle light reflections that may also affect the results, further promoting the relevance of shorter wavelengths. In general, however, comparing the dominant peaks from profilometry and imaging provides additional insight into layer quality. For instance, image power spectral analysis may highlight agglomeration effects at the level of the particle scale, whereas profilometry power spectral analysis might more reliably reveal large-scale surface flaws related to the presence of agglomerate material in front of the blade. The good correlation found for image-based flowability indices and density-based indices for polymers tends to support this view.

Ultimately, the ranking of spreadability depends on the specific index employed. This result confirms that each analytical method probes a distinct aspect of powder behaviour. Therefore, combining at least one density-based parameter with one surface-based parameter provides a more complete representation of powder spreading performance, independently from the powder's material. Despite the inability to define a univocal ranking, metal powder showed generally better spreadability indices. As mentioned above, this result may depend on the internal shear characteristics of powder such as the effective angle of internal friction (Φ_e), reported in Table 4 and representing the effective shear resistance during powder flow, as well as on the particle density that favours the settling of the heavier particles. The spreadability results shown in Table 5, also demonstrated a qualitative association with the cohesion to adhesion ratio (C_s/τ_{ad_s}) values reported in Table 4. However, the present dataset does not allow the independent effects of cohesion and adhesion to be separated. A full understanding of the role of this ratio in powder spreading and final layer quality therefore requires additional studies using systems in which cohesion and adhesion can be varied independently.

5. Conclusion

In this work, the spreadability of two metal powders and two polymeric powders was evaluated using complementary surface- and density-based approaches. Surface topography was characterised by grazing-light image analysis and laser profilometry, while the mass of the deposited powder was used to determine the spread-layer density. The resulting dimensionless indices describe different physical aspects of the powder layer and should therefore not be treated as interchangeable. Their combined use provides complementary information on surface quality and layer packing. The key findings are summarised as follows.:

- Metal powders generally demonstrated superior spreadability compared to polymeric powders across all spreadability indices.
- For the tested powders, spreadability can be explained by the relative values of the effective angle of internal friction (Φ_e) combined with the effect of the different particle densities. However, characterisation of powder flowability also suggests that the cohesion-to-adhesion ratio (C_s/τ_{ad_s}) may play a significant role in powder spreadability.
- Surface roughness parameters in metal powders exhibited a higher sensitivity to spreading speed than those in polymeric powders. This behaviour may be associated with the greater particle mass of the metal powders and the resulting momentum effects during spreading.
- Both image- and profilometer-based spectra covered comparable wavelength ranges. However, profilometer spectra were more frequently multimodal, reflecting their higher sensitivity to absolute height amplitudes. On the other hand, image power spectra enhance the agglomeration analysis at the particle level, producing well-correlated image-based and density-based spreadability indices.
- Overall, increasing spreading speed tended to reduce spreadability, but the magnitude and monotonicity of this effect depended on the material and the selected index, and some variations remained within experimental uncertainty.
- All four powders exhibited wall adhesion greater than internal cohesion under the extrapolated low-stress conditions. The cohesion-to-adhesion ratio ranged from 0.012 to 0.32, indicating material-dependent differences in the relative importance of these two contributions.

These results suggested that the different characterisation methods capture distinct facets of powder layer morphology. Consequently, a hybrid analytical approach is recommended for a comprehensive understanding of powder spreading behaviour. Future research will focus on correlating peak wavelengths and the physical dimensions of surface agglomerates and clusters. Nonetheless, indices derived from power spectra remain highly effective for evaluating surface quality when comparing different process conditions for the same material. A full understanding of the role of the cohesion-to-adhesion ratio in powder spreading and final layer quality requires additional studies using systems in which cohesion and adhesion can be varied independently.

CRediT authorship contribution statement

Bruno Nicola Dose: Writing – review & editing, Writing – original draft, Visualization, Software, Methodology, Investigation, Formal analysis, Data curation. **Sina Zinatlou Ajabshir:** Writing – review & editing, Supervision, Software, Methodology, Data curation, Conceptualization. **Saba Saifoori:** Investigation. **Mozhdeh Mehrabi:** Writing – review & editing, Supervision, Methodology, Investigation, Conceptualization. **Ali Hassanpour:** Writing – review & editing, Validation, Supervision, Resources, Methodology, Formal analysis, Conceptualization. **Diego Barletta:** Writing – review & editing, Supervision, Project administration, Methodology, Funding acquisition, Formal analysis, Conceptualization. **Massimo Poletto:** Writing – review & editing, Validation, Supervision, Project administration, Methodology, Formal analysis, Conceptualization.

Declaration of competing interest

The authors declare that they have no known competing financial interests or personal relationships that could have appeared to influence the work reported in this paper.

Acknowledgment

Bruno Nicola Dose's research grant and part of the research were

supported by European Commission, Next Generation EU - PNRR under project unique No. D42B23001430006.

The authors also gratefully acknowledge Professor Alessandro Ruggiero of the University of Salerno for his valuable insights and suggestions regarding the surface parameters used to assess surface layer quality.

Appendix A. Appendix

The effect of image resolution on the power spectra was assessed by artificially reducing the resolution of one image for each material obtained at 50 mm/s. For each image, the horizontal resolution was reduced from 5739 to 1913 pixels by averaging groups of three adjacent pixels along each row. The reduced-resolution images were then analysed using the same wavelet procedure as the original images. The reduction in resolution shifted the dominant peak towards larger wavelengths, as shown in Table 7

Table 7
Comparison of power spectra's peak wavelengths shift with artificially reduced resolution.

	Original Peak	Shifted Peak
Ti6Al4V	108.7 μm	123.6 μm
AlSi10Mg	124.9 μm	152.1 μm
PA6	345.0 μm	366.0 μm
PA6 Black	282.2 μm	299.4 μm

The shift appears to be larger in metal powders compared to polymeric ones. A secondary effect of the resolution is lowering the power of the peak and producing multiple crossings between the graphs, as shown in Fig. 10.

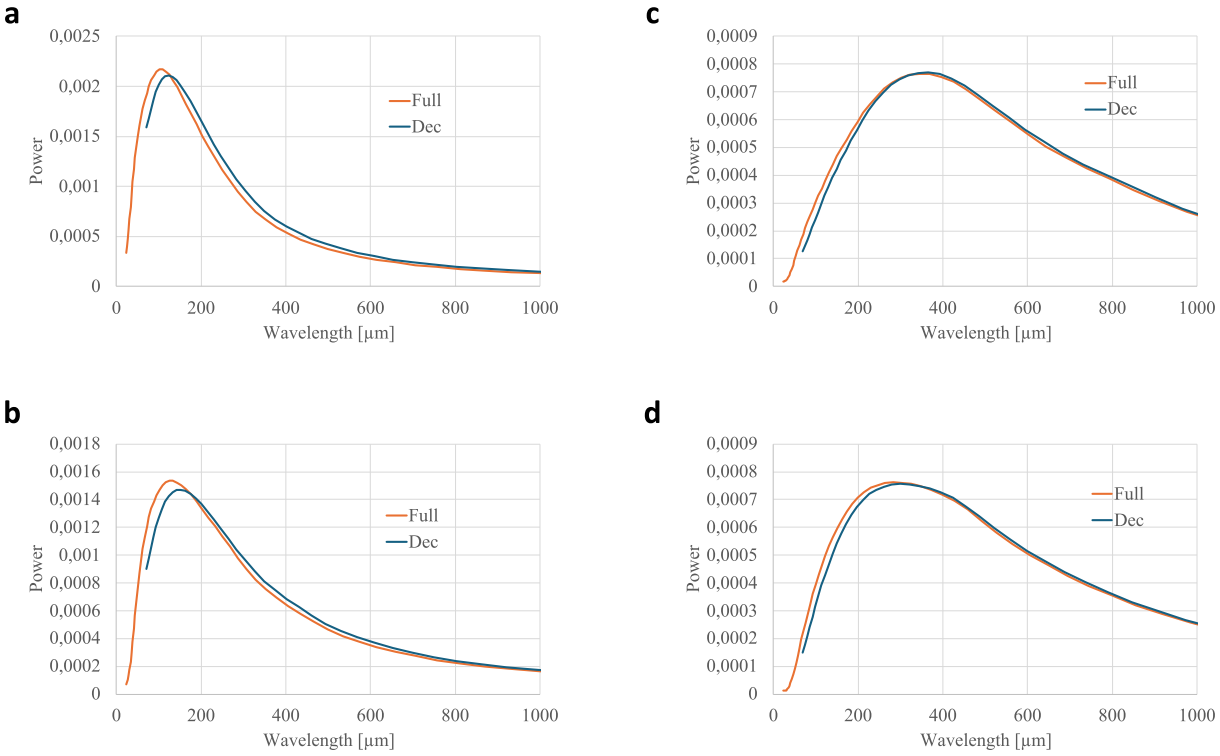


Fig. 10. Effect of artificial decrease in resolution of layers images on image analysis power spectra at a fixed spreading speed of 50 mm/s: a) Ti6Al4V; b) AlSi10Mg; c) PA6; d) PA6 Black.

Appendix B. Supplementary data

Supplementary data to this article can be found online at https://doi.org/10.1016/j.powtec.2026.123301.

Data availability

Data will be made available on request.

References

[1] M. Gopal, H.G. Lemu, E.M. Gutema, Sustainable additive manufacturing and environmental implications: literature review, Sustainability 15 (2022) 504, https://doi.org/10.3390/su15010504.

[2] H. Mohammadkamal, S. Zinatlou Ajabshir, A. Mostafaei, Additive manufacturing at the crossroads: costs, sustainability, and global adoption, J. Manuf. Mater. Proc. 10 (2025) 5, https://doi.org/10.3390/jmmp10010005.

[3] ISO/ASTM 52900:2021(en), Additive Manufacturing — General Principles — Fundamentals and Vocabulary, 2021.

[4] B. Soundararajan, D. Sofia, D. Barletta, M. Poletto, Mesoscale modelling and three-dimensional experimental validation of heat transfer in shallow beds of polyamide powders for laser powder bed fusion, Prog. Addit. Manuf. 10 (2025) 7203–7218, https://doi.org/10.1007/s40964-025-01038-z.

[5] H. Mohammadkamal, F. Caiazzo, The role of laser operation mode on thermal and mechanical behavior in powder bed fusion: a numerical study, Int. J. Adv. Manuf. Technol. (2025), https://doi.org/10.1007/s00170-025-16460-4.

[6] S. Zinatlou Ajabshir, H. Mohammadkamal, Z. Zinatlou Ajabshir, D. Barletta, F. Caiazzo, M. Poletto, Polymeric powders for powder bed fusion: from chemistry and powder characteristics to process parameters, defects and applications, Polymers 18 (2026) 622, https://doi.org/10.3390/polym18050622.

[7] S. Chowdhury, N. Yadaiah, C. Prakash, S. Ramakrishna, S. Dixit, L.R. Gupta, D. Buddhi, Laser powder bed fusion: a state-of-the-art review of the technology, materials, properties & defects, and numerical modelling, J. Mater. Res. Technol. 20 (2022) 2109–2172, https://doi.org/10.1016/j.jmrt.2022.07.121.

[8] L. Hitzler, M. Merkel, W. Hall, A. Öchsner, A review of metal fabricated with laser- and powder-bed based additive manufacturing techniques: process, nomenclature, materials, achievable properties, and its utilization in the medical sector, Adv. Eng. Mater. 20 (2018), https://doi.org/10.1002/adem.201700658.

[9] H. Krueger, Standardization for additive manufacturing in aerospace, Engineering 3 (2017) 585, https://doi.org/10.1016/J.ENG.2017.05.010.

[10] F. Calignano, V. Mercurio, An overview of the impact of additive manufacturing on supply chain, reshoring, and sustainability, Clean. Logist. Supply Chain 7 (2023) 100103, https://doi.org/10.1016/j.clscn.2023.100103.

[11] A. Boschetto, L. Bottini, S. Vatanparast, Powder bed monitoring via digital image analysis in additive manufacturing, J. Intell. Manuf. 35 (2024) 991–1011, https://doi.org/10.1007/s10845-023-02091-7.

[12] M. Tang, Y. Guo, W. Zhang, H. Ma, L. Yang, W. Wei, L. Wang, S. Fan, Q. Zhang, On recoated powder quality with a forward rotating flexible roller in laser powder bed fusion of 30 wt% 5 μm SiCp/AlSi10Mg composites, Mater. Des. 225 (2023) 111489, https://doi.org/10.1016/j.matdes.2022.111489.

[13] M. Mehrabi, J. Gardy, F.A. Talebi, A. Farshchi, A. Hassanpour, A.E. Bayly, An investigation of the effect of powder flowability on the powder spreading in additive manufacturing, Powder Technol. 413 (2023) 117997, https://doi.org/10.1016/j.powtec.2022.117997.

[14] L. Cordova, T. Bor, M. de Smit, M. Campos, T. Tinga, Measuring the spreadability of pre-treated and moisturized powders for laser powder bed fusion, Addit. Manuf. 32 (2020) 101082, https://doi.org/10.1016/j.addma.2020.101082.

[15] M. Lupo, S.Z. Ajabshir, D. Sofia, D. Barletta, M. Poletto, Experimental metrics of the powder layer quality in the selective laser sintering process, Powder Technol. 419 (2023) 118346, https://doi.org/10.1016/j.powtec.2023.118346.

[16] M. Lupo, S. Zinatlou Ajabshir, D. Sofia, D. Barletta, M. Poletto, Discrete element method model calibration and validation for the spreading step of the powder bed fusion process to predict the quality of the layer surface, Particuology 94 (2024) 261–273, https://doi.org/10.1016/j.partic.2024.08.010.

[17] A. Mussatto, R. Groarke, A. O'Neill, M.A. Obeidi, Y. Delaure, D. Brabazon, Influences of powder morphology and spreading parameters on the powder bed topography uniformity in powder bed fusion metal additive manufacturing, Addit. Manuf. 38 (2021) 101807, https://doi.org/10.1016/j.addma.2020.101807.

[18] S. Zinatlou Ajabshir, C. Hare, D. Sofia, D. Barletta, M. Poletto, Investigating the effect of temperature on powder spreading behaviour in powder bed fusion additive manufacturing process by Discrete Element Method, Powder Technol. 436 (2024) 119468, https://doi.org/10.1016/j.powtec.2024.119468.

[19] N. Hantke, T.R. Brocksieper, T. Grimm, J.T. Sehrt, Influence of recoater speed on powder bed and part quality in powder bed fusion of metals using a laser beam, Metals (Basel) 15 (2025) 225, https://doi.org/10.3390/met15030225.

[20] S. Zinatlou Ajabshir, C. Hare, D. Barletta, M. Poletto, Discrete element method study on spreading behaviour of non-spherical polymeric powder in powder bed fusion with blade and roller spreaders, Chem. Eng. Trans. 117 (2025) 787–792, https://doi.org/10.3303/CET25117132.

[21] S. Zinatlou Ajabshir, C. Hare, D. Barletta, M. Poletto, Assessment of the powder spreading parameters for non-spherical polymeric powder used in powder bed fusion process: a DEM simulation study, Addit. Manuf. 119 (2026) 105099, https://doi.org/10.1016/j.addma.2026.105099.

[22] L. Haferkamp, L. Haudenschild, A. Spierings, K. Wegener, K. Riener, S. Ziegelmeier, G.J. Leichtfried, The influence of particle shape, powder flowability, and powder layer density on part density in laser powder bed fusion, Metals (Basel) 11 (2021) 418, https://doi.org/10.3390/met11030418.

[23] T. Zhang, D. Chen, H. Yang, W. Zhao, Y. Wang, H. Zhou, Spreading behavior of non-spherical particles with reconstructed shapes using discrete element method in additive manufacturing, Polymers 16 (2024) 1179, https://doi.org/10.3390/polym16091179.

[24] W. Nan, Y. Gu, Experimental investigation on the spreadability of cohesive and frictional powder, Adv. Powder Technol. 33 (2022) 103466, https://doi.org/10.1016/j.apt.2022.103466.

[25] F.A. Talebi, Z. Haydari, H. Salehi, M. Mehrabi, J. Gardy, M. Bradley, A.E. Bayly, A. Hassanpour, Spreadability of powders for additive manufacturing: a critical review of metrics and characterisation methods, Particuology 93 (2024) 211–234, https://doi.org/10.1016/j.partic.2024.06.013.

[26] Test Method for Tap Density of Metal Powders and Compounds, 2024, https://doi.org/10.1520/B0527-24.

[27] H. Chen, Q. Wei, Y. Zhang, F. Chen, Y. Shi, W. Yan, Powder-spreading mechanisms in powder-bed-based additive manufacturing: experiments and computational modeling, Acta Mater. 179 (2019) 158–171, https://doi.org/10.1016/j.actamat.2019.08.030.

[28] M. Rüther, S.H. Klippstein, S. Ponusamy, T. Rüther, H.-J. Schmid, Flowability of polymer powders at elevated temperatures for additive manufacturing, Powder Technol. 422 (2023) 118460, https://doi.org/10.1016/j.powtec.2023.118460.

[29] S. Yim, H. Bian, K. Aoyagi, K. Yamanaka, A. Chiba, Spreading behavior of Ti–48Al–2Cr–2Nb powders in powder bed fusion additive manufacturing process: experimental and discrete element method study, Addit. Manuf. 49 (2022) 102489, https://doi.org/10.1016/j.addma.2021.102489.

[30] M. Markl, M.R. Azadi Tinat, T. Berger, J. Renner, C. Körner, Extracting powder bed features via electron optical images during electron beam powder bed fusion, Addit. Manuf. Lett. 10 (2024) 100220, https://doi.org/10.1016/j.addlet.2024.100220.

[31] R.W. Penny, D. Oropeza, P.M. Praegla, R. Weissbach, C. Meier, W.A. Wall, A. John Hart, Quantitative analysis of thin metal powder layers via transmission X-ray imaging and discrete element simulation: blade-based spreading approaches, Powder Technol. 432 (2024) 119106, https://doi.org/10.1016/j.powtec.2023.119106.

[32] M.H. Sehhat, A. Mahdianikhotbesara, Powder spreading in laser-powder bed fusion process, Granul. Matter 23 (2021) 89, https://doi.org/10.1007/s10035-021-01162-x.

[33] H. Salehi, J. Cummins, E. Gallino, N. Harrison, A. Hassanpour, M. Bradley, A new approach to quantify powder's bed surface roughness in additive manufacturing, Powder Technol. 407 (2022) 117614, https://doi.org/10.1016/j.powtec.2022.117614.

[34] S. Zinatlou Ajabshir, D. Sofia, C. Hare, D. Barletta, M. Poletto, Experimental characterisation of the spreading of polymeric powders in powder bed fusion additive manufacturing process at changing temperature conditions, Adv. Powder Technol. 35 (2024) 104412, https://doi.org/10.1016/j.apt.2024.104412.

[35] L.C. Capozzi, A. Sivo, E. Bassini, Powder spreading and spreadability in the additive manufacturing of metallic materials: a critical review, J. Mater. Process. Technol. 308 (2022) 117706, https://doi.org/10.1016/j.jmatprotec.2022.117706.

[36] S. Brenner, M. Moser, L. Strauß, V. Nedeljkovic-Groha, G. Löwisch, Recoater crashes during powder bed fusion of metal with laser beam: simulative prediction of interference and experimental evaluation of resulting part quality, Prog. Addit. Manuf. 8 (2023) 759–768, https://doi.org/10.1007/s40964-023-00471-2.

[37] A. Boschetto, L. Bottini, S. Vatanparast, F. Veniali, Part defects identification in selective laser melting via digital image processing of powder bed anomalies, Prod. Eng. 16 (2022) 691–704, https://doi.org/10.1007/s11740-022-01112-3.

[38] W. Nan, M. Pasha, T. Bonakdar, A. Lopez, U. Zafar, S. Nadimi, M. Ghadiri, Jamming during particle spreading in additive manufacturing, Powder Technol. 338 (2018) 253–262, https://doi.org/10.1016/j.powtec.2018.07.030.

[39] B.N. Dose, S.Z. Ajabshir, A. Hassanpour, D. Barletta, M. Poletto, The impact of powder delivery process parameters on spreading behaviour in powder bed fusion additive manufacturing, Chem. Eng. Trans. 117 (2025) 793–798, https://doi.org/10.3303/CET25117133.

[40] DIN EN ISO 25178-2:2023-09, Geometrische Produktspezifikation_(GPS)_-Oberflächenbeschaffenheit: Flächenhaft_- Teil_2: Begriffe und Kenngrößen für die Oberflächenbeschaffenheit (ISO_25178–2:2021); Deutsche Fassung EN_ISO_25178-2:2022, 2023, https://doi.org/10.31030/3294021.

[41] DIN EN ISO 4287:2010-07, Geometrische Produktspezifikation (GPS)_-Oberflächenbeschaffenheit: Tastschnittverfahren_- Benennungen, Definitionen und Kenngrößen der Oberflächenbeschaffenheit (ISO_4287:1997_+ Cor_1:1998_+ Cor_2:2005_+ Amd_1:2009); Deutsche Fassung EN_ISO_4287:1998_+ AC:2008_+ A1:2009, 2010, https://doi.org/10.31030/1699310.

[42] A.W. Jenike, Storage and Flow of Solids, Bulletin No. 123; Vol. 53, No. 26, 1964, U. S. Department of Energy, 1976, https://doi.org/10.2172/5240257.

[43] D. Ruggi, M. Lupo, D. Sofia, C. Barrès, D. Barletta, M. Poletto, Flow properties of polymeric powders for selective laser sintering, Powder Technol. 370 (2020) 288–297, https://doi.org/10.1016/j.powtec.2020.05.069.

[44] S. Yim, H. Wang, K. Aoyagi, K. Yamanaka, A. Chiba, Role of gravity magnitude on flowability and powder spreading in the powder bed fusion additive manufacturing process: towards additive manufacturing in space, Addit. Manuf. 94 (2024) 104441, https://doi.org/10.1016/j.addma.2024.104441.

[45] K. Janzen, K.J. Kallies, L. Waalkes, P. Imgrund, C. Emmelmann, Influence of different powder conditioning strategies on metal binder jetting with Ti-6Al-4V, Materials (Basel, Switzerland) 17 (2024) 750, https://doi.org/10.3390/ma17030750.

[46] Y.M. Fouda, A.E. Bayly, A DEM study of powder spreading in additive layer manufacturing, Granul. Matter 22 (2020) 10, https://doi.org/10.1007/s10035-019-0971-x.

[47] S. Yim, K. Aoyagi, H. Bian, Y. Cui, A. Chiba, Factors determining the flowability and spreading quality of gas-atomized Ti-48Al-2Cr-2Nb powders in powder bed fusion additive manufacturing, Powder Technol. 412 (2022) 117996, https://doi.org/10.1016/j.powtec.2022.117996.

[48] F. Sillani, R. Schiegg, M. Schmid, E. MacDonald, K. Wegener, Powder surface roughness as proxy for bed density in powder bed fusion of polymers, Polymers 14 (2021) 81, https://doi.org/10.3390/polym14010081.

[49] K. singh Randhawa, Hygroscopic behaviour analysis of biocompatible PA6 and PA6 composites containing oxide and nitride compounds of boron, Ceram. Int. 48 (2022) 29340–29348, https://doi.org/10.1016/j.ceramint.2022.05.370.

[50] R. Xu, W. Nan, Analysis of the metrics and mechanism of powder spreadability in powder-based additive manufacturing, Addit. Manuf. 71 (2023), https://doi.org/10.1016/j.addma.2023.103596.

[51] M.Y. Shaheen, A.R. Thornton, S. Luding, T. Weinhart, The influence of material and process parameters on powder spreading in additive manufacturing, Powder Technol. 383 (2021) 564–583, https://doi.org/10.1016/j.powtec.2021.01.058.
[52] D. Yao, X. An, H. Fu, H. Zhang, X. Yang, Q. Zou, K. Dong, Dynamic investigation on the powder spreading during selective laser melting additive manufacturing, Addit. Manuf. 37 (2021) 101707, https://doi.org/10.1016/j.addma.2020.101707.
[53] S. Zinatlou Ajabshir, D. Barletta, M. Poletto, The effect of process conditions on powder flow properties for slow flow regimes, Kona Powder Part. J. 42 (2025) 2025006, https://doi.org/10.14356/kona.2025006.